SEL1L-HRD1 ER-Associated Degradation Facilitates Prohormone Convertase 2 Maturation and Glucagon Production in Islet α Cells

Wenzhen Zhu[1], Linxiu Pan[1,2], Xianwei Cui[3], Anna Chiara Russo[1], Rohit Ray[1], Brent Pederson[1,3], Xiaoqiong Wei[2,3], Liangguang Leo Lin[2,3], Hannah Hafner[4], Brigid Gregg[4,5], Neha Shrestha[1,3], Chengyang Liu[6], Ali Naji[6], Peter Arvan[1,3], Darleen A. Sandoval[7,8], Iris Lindberg[9], Ling Qi[1,2,3*], and Rachel B. Reinert[1*]

[1] Division of Metabolism, Endocrinology & Diabetes, Department of Internal Medicine, University of Michigan Medical School, Ann Arbor, MI 48105, USA;

[2] Present address: Department of Molecular Physiology and Biological Physics, University of Virginia School of Medicine, Charlottesville, VA 22903, USA;

[3] Department of Molecular & Integrative Physiology, University of Michigan Medical School, Ann Arbor, MI 48105, USA;

[4] Department of Pediatrics, Division of Pediatric Endocrinology, University of Michigan, Ann Arbor, MI 48105, USA;

[5] Department of Nutritional Sciences, School of Public Health, University of Michigan, Ann Arbor, MI 48105, USA;

[6] Department of Surgery, Perelman School of Medicine, University of Pennsylvania, Philadelphia, Pennsylvania, USA;

[7] Department of Surgery, University of Michigan, Ann Arbor, MI 48109, USA;

[8] Department of Pediatrics, Nutrition Section, University of Colorado Anschutz Medical Campus, Aurora, CO 80045, USA;

[9] Department of Anatomy and Neurobiology, University of Maryland-Baltimore, Baltimore, MD 21201, USA

*** Correspondence:**

Rachel Reinert, MD, PhD, 734-232-1715, reinertr@med.umich.edu;

Ling Qi, PhD, 734-417-5447, xvr2hm@virginia.edu

Conflict of Interest Statement: The authors have declared that no conflict of interest exists.

Running title: A key role of SEL1L-HRD1 ERAD in proPC2 maturation in α cells

Keywords: SEL1L-HRD1 ERAD, ER, protein folding, protein degradation, proPC2, PC2, proglucagon, glucagon

ABSTRACT

Proteolytic cleavage of proglucagon by prohormone convertase 2 (PC2) is required for islet α cells to generate glucagon. However, the regulatory mechanisms underlying this process remain largely unclear. Here, we report that SEL1L-HRD1 endoplasmic reticulum (ER)-associated degradation (ERAD), a highly conserved protein quality control system responsible for clearing misfolded proteins from the ER, plays a key role in glucagon production by regulating turnover of the nascent proform of the PC2 enzyme (proPC2). Using a mouse model with SEL1L deletion in proglucagon-expressing cells, we observed a progressive decline in stimulated glucagon secretion and a reduction in pancreatic glucagon content. Mechanistically, we found that endogenous proPC2 is a substrate of SEL1L-HRD1 ERAD, and that degradation of misfolded proPC2 ensures the maturation of activation-competent proPC2 protein. These findings identify ERAD as a novel regulator of PC2 biology and an essential mechanism for maintaining α cell function.

INTRODUCTION

Diabetes mellitus encompasses a spectrum of metabolic diseases with dysregulated secretion of insulin and glucagon from pancreatic islet β and α cells as a central feature. Interest in α cell biology has been reinvigorated in recent years, particularly with the advent of specific tools to manipulate α cell gene expression and glucagon signaling (1-3). Hyperglucagonemia is observed in both type 1 and type 2 diabetes, contributing to hyperglycemia (4, 5). Glucagon receptor antagonists are in clinical development to improve hyperglycemia in diabetes (6-8), but may trigger dramatic α cell hyperplasia (9) like that observed in models with genetic deletion of glucagon (10) or its receptor (*Gcgr*) (11). Conversely, recent studies have demonstrated a more positive role for α cells in directly promoting β cell function and survival through secretion of proglucagon-derived peptides such as glucagon and/or glucagon-like peptide 1 (GLP-1) and their interaction with GCGR and GLP1R receptors on β cells (12-15). The cellular mechanisms that define the ability of α cells to regulate the production and maturation of proglucagon-derived peptides remains an active area of investigation.

In α cells, proglucagon undergoes limited proteolysis primarily by prohormone convertase 2 (PC2), which generates glucagon as the major peptide product (16). PC2 is initially synthesized and folded as a 75 kDa inactive zymogen, proPC2, in the endoplasmic reticulum (ER). The maturation of proPC2 to its ~64 kDa active form, PC2, is a complex, multi-step process that requires folding in the ER, posttranslational modification in the Golgi network, and sorting into acidic secretory granules, where it is then activated by intramolecular autocatalysis (17, 18). Understanding the regulatory mechanisms underlying proPC2 maturation and processing is essential for optimizing glucagon production and developing targeted therapeutic strategies for manipulating α cell function.

The synthesis and packaging of islet hormones and their processing enzymes into secretory granules depends on effective protein quality systems, particularly within the ER. Genome-wide association studies (reviewed in (19)) and multi-omic analyses of human islets (20) have linked genes involved in ER homeostasis and ER stress responses with both type 1 and type 2 diabetes, but many of these underlying mechanisms have primarily been studied in β cells (21, 22). The specific mechanisms defining ER homeostasis in α cells are poorly understood. As the initial location of protein synthesis, the ER must maintain a healthy environment for proteins to fold into their mature structure, as failure to do so risks pathologic aggregation or premature activation. Cells employ multiple, interrelated quality control mechanisms to respond to the ever-

changing burden of protein synthesis and manage protein misfolding, including the unfolded protein response (UPR), autophagy, and ER-associated degradation (ERAD) (23).

ERAD is a key quality control mechanism responsible for targeting misfolded proteins in the ER for cytosolic proteasomal degradation (24, 25). The SEL1L-HRD1 protein complex represents the most conserved branch of ERAD, where SEL1L serves as a cognate cofactor for the E3 ligase HRD1 (26, 27). We and others have shown that SEL1L controls both HRD1 protein stability (28, 29) and ERAD complex formation (30, 31). SEL1L-HRD1 ERAD promotes the maturation of several misfolding-prone prohormones, such as pro-arginine vasopressin (proAVP) and pro-opiomelanocortin (POMC) in neurons (32, 33). In the absence of SEL1L, proAVP and POMC peptides aggregate in the ER, impairing their maturation and limiting production of their functional hormone derivatives. In pancreatic islet β cells, SEL1L-HRD1 ERAD is critical to maintain cell identity (34, 35) and insulin production (36, 37). The role of SEL1L-HRD1 ERAD in islet α cells and proglucagon maturation has until now been unexplored.

In this study, we generated a mouse model inactivating *Sel1L* in proglucagon-expressing cells and found that defective ERAD is associated with impaired glucagon production secondary to impaired maturation of proPC2. Mechanistically, we uncovered an unexpected role of SEL1L-HRD1 ERAD in the quality control of proPC2 in the ER – ensuring that misfolded proPC2 is targeted for degradation, thereby maintaining the integrity of proglucagon processing machinery. In the absence of proper ERAD function, misfolded proPC2 accumulates in the ER, undergoes aberrant proteolytic cleavage and forms high molecular weight disulfide-bonded complexes, leading to impaired maturation and reduced levels of active PC2. This, in turn, limits the cleavage of proglucagon, resulting in diminished glucagon production and secretion.

RESULTS

The ER network and SEL1L-HRD1 ERAD expression in mouse and human islet α cells

Like islet β cells (34, 35), neighboring α cells also have an expansive network of ER, as observed by transmission electron microscopy (TEM) (Fig. 1A, Fig. S1A). To explore the role of ER homeostasis in α cells, we examined the ER in glucagon-null *Gcg*-STOP-flox ("*Gcg*$^{-/-}$") mice (38). In this model, there is a dramatic expansion of the α cell population secondary to hyperaminoacidemia, due to the complete absence of hepatic glucagon signaling (39, 40). Despite their inability to make proglucagon and its derivative peptides, the ER remained

prominent in *Gcg*$^{-/-}$ α cells (Fig. 1B, Fig. S1A-B). Using confocal microscopy, we found that protein levels of BiP, an ER chaperone protein, is relatively low in normal α cells compared to that in β cells in wild-type mice (Fig. 1C-D). However, BiP was increased in α cells in *Gcg*$^{-/-}$ mice (Fig. 1C-D). This expansion of ER capacity in *Gcg*$^{-/-}$ α cells was also reflected by increased expression of SEL1L compared to that in normal α cells (Fig. 1E-F, white arrows). SEL1L was expressed in both α and β cells in human islets, from donors with or without diabetes (Fig. 1G). These findings led us to investigate the role of SEL1L-HRD1 ERAD in α cell ER homeostasis and function.

Targeted deletion of SEL1L in islet α cells

To define the role of SEL1L-HRD1 ERAD in α cells, we developed a mouse model in which SEL1L was inactivated specifically in proglucagon-expressing cells by crossing mice expressing an "improved" constitutively active Cre recombinase under the proglucagon promoter (*Gcg*^{iCre}) (41) with Sel1L-floxed mice on a B6 background (28). In these *Sel1L*$^{\Delta Gcg}$ mice, almost all α cells showed absence of immunolabeling for SEL1L (Fig. 2A). Confirming that ERAD function was impaired in *Sel1L*$^{\Delta Gcg}$ α cells, we also observed increased expression of the ERAD substrate OS9 (Fig. 2B) and the ER chaperone BiP (Fig. 2C). By contrast, immunofluorescence of glucagon was slightly reduced in *Sel1L*$^{\Delta Gcg}$ α cells (Fig. 2D), suggesting that ERAD impairs glucagon production. However, this appears to occur through an indirect mechanism, as ERAD dysfunction did not lead to accumulation of proglucagon in the ER (Fig. 2D), as has been shown with other misfolding-prone prohormones such as proAVP and POMC (32, 33).

Despite targeting SEL1L deletion in all proglucagon-expressing cells in *Sel1L*$^{\Delta Gcg}$ mice, we did not observe increased BiP expression in intestinal L-cells (Fig. S2A), as detected by an anti-glucagon antibody that shows colocalization with anti-GLP-1 antibody (Fig. S2B). To better understand the extent of Cre recombinase activity in this model, we generated *R26R-EYFP*$^{\Delta Gcg}$ reporter mice by crossing the *ROSA26*-STOP-flox-EYFP (42) with the same *Gcg*^{iCre} line (41). We found that the vast majority of islet α cells expressed the YFP reporter (Fig. S2C), while YFP was not detected in intestinal L-cells (Fig. S2D). In line with this notion, there was no difference in glucose-stimulated total GLP-1 levels in serum (Fig. S2F) or in GLP-1 content of distal colon epithelium (Fig. S2G) from *Sel1L*$^{\Delta Gcg}$ mice. Together, these data suggest that this *Gcg*^{iCre} line predominantly targets islet α cells.

Attenuated glucagon production in *Sel1L$^{\Delta Gcg}$* mice

We next asked how inactivation of SEL1L-HRD1 ERAD affected α cell function. Male and female *Sel1L$^{\Delta Gcg}$* mice showed normal growth on chow diet through adulthood (Fig. 3A). There was no change in oral glucose tolerance (Fig. 3B) in 4-8 month-old *Sel1L$^{\Delta Gcg}$* mice compared to sex-matched littermate controls. To assess stimulated glucagon secretion *in vivo*, we subjected adult cohorts to insulin-induced hypoglycemia. At 4-8 months of age, male *Sel1L$^{\Delta Gcg}$* mice had significantly decreased glucagon secretion following hypoglycemia (Fig. 3C). Female *Sel1L$^{\Delta Gcg}$* mice also showed reduced glucagon secretion *in vivo*, but starting at 8 months of age (Fig. 3C).

To understand the mechanism underlying lower glucagon levels in *Sel1L$^{\Delta Gcg}$* mice, we next investigated glucagon production and secretion in α cells. In both adult male and female *Sel1L$^{\Delta Gcg}$* mice, pancreatic glucagon content was reduced by half by 4 months of age (Fig. 3D), as detected by an ELISA assay targeted to detect the N- and C-terminal ends of the mature 29-amino acid glucagon peptide. The defect in circulating glucagon levels was not due to defects in secretory dynamics or response to stimuli, as isolated islets from *Sel1L$^{\Delta Gcg}$* mice showed a similar secretory response to low glucose with or without the secretagogue L-arginine, when normalized to total glucagon content (Fig. 3E). Importantly, the expression of Cre in the native *Gcg* locus did not affect pancreatic glucagon content in *R26R-EYFP$^{\Delta Gcg}$* reporter mice (Fig. S2E). Altogether, these data suggest that ERAD dysfunction limits glucagon production in α cells, while having no effect on glucagon secretory dynamics.

ER dilation in *Sel1L$^{\Delta Gcg}$* α cells

We next performed TEM to examine α cell morphology and secretory granule formation. In contrast to the prominent stacks of ER and abundant electron-dense granules in normal α cells, the α cells in *Sel1L$^{\Delta Gcg}$* mice showed significant ER dilation and, in extreme cases, fewer glucagon granules (Fig. 3F and S3A). Nonetheless, the glucagon granules in *Sel1L$^{\Delta Gcg}$* α cells appeared largely normal in morphology (Fig. 3F and S3A). Additionally, β cell architecture and pancreatic insulin content were unchanged in *Sel1L$^{\Delta Gcg}$* mice (Fig. S3B-C). By immunofluorescence detection with antibodies to the mature glucagon sequence, α cell mass was reduced in adult *Sel1L$^{\Delta Gcg}$* mice (Fig. S3D), but without significant changes in α cell apoptosis (Fig. S3E) or proliferation (Fig. S3F), as evaluated by TUNEL assay and Ki67+ cells, respectively. Altogether, these data suggest that ERAD deficiency causes ER dilation and limits production of mature glucagon in α cells.

ERAD deficiency causes the accumulation of proPC2 protein in vivo

Given the greater reduction in mature glucagon relative to proglucagon levels in *Sel1L*$^{\Delta Gcg}$ α cells, we speculated that the defect may lie in the proteolytic cleavage of proglucagon, a process catalyzed by the PC2 enzyme. PC2 is initially synthesized in the ER as the zymogen proPC2. ProPC2 initially folds in the ER, forming three disulfide bonds (Fig. 4A) and becomes activated within secretory granules (43), where the Pro domain is cleaved from the proprotein by autocatalysis. AlphaFold structure modeling was used to visualize the possible conformation of each domain (Fig. 4B). This tertiary structure aligns with prior work showing that proPC2 is susceptible to misfolding and aggregation within the ER in the absence of its chaperone protein 7B2 (44). We thus asked how SEL1L-HRD1 ERAD affects PC2 biology.

To visualize the expression level and distribution of proPC2 in vivo, we performed immunofluorescence labeling using antibodies specific for different regions of proPC2 (45) (Fig. 4A). There was a marked increase in proPC2 levels in *Sel1L*$^{\Delta Gcg}$ α cells (Fig. 4C). In line with this finding, immunolabeling with antibodies to the catalytic domain of PC2 (which detects both mature PC2 and the proPC2 protein) showed that total PC2 levels were also significantly increased in *Sel1L*$^{\Delta Gcg}$ α cells (Fig. 4D). These data suggest that SEL1L deficiency causes the accumulation of proPC2 protein in vivo.

Altered proPC2 processing in the absence of SEL1L-HRD1 ERAD

To further explore how SEL1L-HRD1 ERAD regulates proPC2 maturation in α cells, we developed a cell culture model of ERAD deficiency using CRISPR-mediated deletion of either SEL1L or HRD1 in the well-established αTC1-6 α cell line (ΔSel1L and ΔHrd1, respectively) (Fig. 5A, Fig. S4A-C). Deletion of SEL1L or HRD1 in αTC1-6 cells caused ERAD dysfunction, as demonstrated by increased protein levels of ERAD substrates IRE1α and OS9 (Fig. S4D-F). In addition, ERAD deficiency triggered a mild activation of ER stress responses as measured by the phosphorylation of eIF2α and splicing of *Xbp1* mRNA (Fig. S4G-K). Compared to cells treated with the ER stressor tunicamycin, the level of *Xbp1* mRNA splicing in ERAD-deficient αTC1-6 cells was modest (Fig. S4K), similar to our previous observations (33, 34).

We then examined (pro)PC2 expression using Western blot with three different antibodies targeted to different regions of the polypeptide (Fig. 4A). Using a proPC2-specific antibody, we found that expression of proPC2 protein (~75 kDa) was significantly increased in both ΔSel1L and ΔHrd1 α cells compared to control cells (Fig. 5B). Intriguingly, we observed a novel ~55

kDa proPC2 fragment (proPC2*) that was highly enriched in ERAD-deficient cells (Fig. 5B). In addition, using an antibody targeting the PC2 catalytic domain, we confirmed the accumulation of proPC2 and proPC2* in both ΔSel1L and ΔHrd1 α cells compared to control cells, while mature PC2 (~64 kDa) protein levels were reduced by half (Fig. 5C). In contrast, using an antibody specific for the C-terminal domain of PC2, we failed to observe proPC2* (Fig. 5D), suggesting that proPC2* was generated by an aberrant cleavage at the C-terminal end of the protein. We confirmed that proPC2* was derived from proPC2 given its absence in cells with CRISPR-mediated co-deletion of PC2 and Sel1L (Fig. 5E-F).

The accumulation of both proPC2 and proPC2* was specific to ERAD deficiency, and uncoupled from ER stress, as it was not observed in control αTC1-6 cells following induction of ER stress with either tunicamycin or thapsigargin (Fig. 5G). Importantly, ERAD deficiency was associated with a slight decrease, not increase, in expression of *Pcsk2* mRNA (Fig. 5H). Therefore, the accumulation of proPC2 protein was attributed to post-transcriptional regulation. Taken together, these data show that SEL1L-HRD1 ERAD is critical for the maturation of proPC2 in α cells by preventing its abnormal proteolytic cleavage.

Nascent proPC2 is degraded by SEL1L-HRD1 ERAD in α cells

We then explored the molecular mechanism underlying the interplay between ERAD and proPC2. Using cycloheximide to block protein synthesis, we found that both proPC2 and proPC2* were stabilized in both ΔSel1L and ΔHrd1 α cells, as validated by two different antibodies (Fig. 6A-B). Moreover, in the absence of ERAD, proPC2 formed high molecular weight (HMW) protein complexes as visualized by non-reducing SDS-PAGE. The formation of these HMW complex were mediated by aberrant disulfide bonds as they were sensitive to the reducing agent β-mercaptoethanol (lanes 5-6 vs. lanes 2-3, Fig. 6C). Strikingly, the proPC2* fragment contributed to this process, as it co-migrated with HMW aggregates under non-reducing conditions (lanes 5-6 vs. lanes 2-3, Fig. 6C). Supporting the direct role of SEL1L-HRD1 ERAD in regulating proPC2 degradation, we found that proPC2 was polyubiquitinated in a HRD1-dependent manner (Fig. 6D). MG132 treatment also increased the polyubiquitination of proPC2 (lanes 4-5, Fig. 6D), pointing to the involvement of proteasome. Interestingly, MG132 treatment also increased the production of proPC2* in control cells (input lane 4 vs. input lanes 1-2, Fig. 6D). This suggests that proPC2* is routinely generated in normal α cells but is undetectable due to degradation by SEL1L-HRD1 ERAD. These data demonstrate that in the

absence of SEL1L-HRD1 ERAD, proPC2 accumulates in α cells, is abnormally cleaved, and forms HMW complexes via aberrant disulfide bonds.

Impaired proPC2 enzymatic activity in ERAD-deficient α cells

One unique feature of PC2 is its requirement for a protein cofactor, 7B2 (also called secretogranin-5), to serve as a chaperone that binds proPC2 in the ER and inhibits PC2 enzyme activation until it reaches later stages in the secretory pathway (45). We found that 7B2 protein expression was reduced in both ΔSel1L and ΔHrd1 α cells compared to their respective controls (Fig. 6E). To determine whether these changes in proPC2 and 7B2 affected PC2 enzymatic function, we measured PC2 activity in αTC cells using a substrate-specific aminomethylcoumarin assay as previously described (46). This assay detects activity of mature PC2 in addition to properly folded proPC2 that is spontaneously autoactivated in the low pH of the reaction buffer (18). Compared to control cells, ΔSel1L and ΔHrd1 αTC cells showed significantly impaired PC2 activity (Fig. 6F). Addition of the 7B2 C-terminal peptide, a potent and specific PC2 inhibitor (46), successfully abolished PC2 activity in all cells as a control (Fig. 6F). Together, these data suggest that the aberrant cleavage and aggregation of proPC2 in ERAD-deficient α cells impairs PC2 activity.

DISCUSSION

In this study, we report a novel function of SEL1L-HRD1 ERAD in regulation of islet α cell function. We found that SEL1L-HRD1 ERAD is essential for efficient glucagon biogenesis by facilitating the folding and maturation of nascent proPC2 in the ER. Indeed, ERAD deficiency causes accumulation of aberrantly cleaved proPC2* and aggregation of proPC2-derived proteins, leading to reduced production and activity of mature PC2, and consequently, impaired proglucagon processing in α cells (Figure 7). This study reveals a novel regulatory mechanism for regulation of PC2 function in neuroendocrine cells.

ER proteostasis is critical for optimal protein synthesis and secretion, a primary function of islet endocrine cells. Failure of islet β cells to adapt to ER dysfunction during metabolic stress has been implicated as a key factor in diabetes pathogenesis (23), but the relative role of the ER homeostasis in α cell function had not been rigorously studied. Here, we found that ER volume is increased in the expanded α cell population in *Gcg*$^{-/-}$ mice, in which the complete absence of hepatic glucagon signaling leads to hyperaminoacidemia, providing a strong stimulus for α cell

proliferation (39, 40). ER volume expansion has been observed in β cells from mice and humans with diabetes (47, 48) as an adaptation to the demand for increased insulin production (22). As glucagon, the primary α cell peptide product, is not produced in *Gcg*$^{-/-}$ mice, it is possible that the ER expansion in this model is not solely triggered by a demand for increased protein synthesis but is instead attributable to the ER's role in supplying lipids for cell membrane expansion and growth (49). Nevertheless, we presume that ER volume expansion would also be found in normal α cells exposed to genetic or pharmacologic glucagon receptor inhibition, and that these α cells would be predisposed to even higher demands on the ER, as (pro)glucagon production is increased in *Gcgr*$^{-/-}$ mouse models (50) and in humans with GCGR mutations (51) or treated with GCGR inhibitors (52, 53).

Our understanding of the mechanisms promoting α cell ER homeostasis or ER stress remains limited. Human α cells were more resistant to inflammatory stressors that cause β cell death, despite induction of similar ER stress markers like *Ddit3* (CHOP) and *Xbp1s* (54). Similarly, iPSC-derived α cells were more resilient to ER stress-induced apoptosis in an in vitro model of type 1 diabetes (55). A recent analysis of single cell RNAseq data from human islets demonstrated increased activation of ER stress-related pathways in α cells from patients with type 1, but not type 2, diabetes (56). Mouse models interrogating ER function in α cells have focused on the unfolded protein response (UPR), demonstrating distinct effects of each branch on α cell function. Germline deletion of PERK, the defective eIF2α kinase in the diabetes-causing Wolcott-Rallison syndrome, resulted in early loss of both β and α cell mass (57). In contrast, deletion of the IRE1α effector Xbp1 in α cells led to ER dilation and glucose intolerance in older adult mice, attributed to α cell insulin resistance causing impaired suppression of glucagon secretion (58). The phenotypes observed in mouse models with defects in the α cell UPR are quite distinct from that of ERAD deficiency, as we have reported in other cell types – but these systems likely work in cooperation, and the ability to use compensatory mechanism(s) will determine the cell's ultimate response to a given stress (23, 26, 59). For example, it remains to be determined whether the modest activation of UPR signaling in ERAD-deficient α cells, particularly through the ERAD substrate and UPR sensor IRE1α, plays any compensatory role (positive or negative) in responding to the ER defects in this model.

Islet α cells are inherently challenging to study, not only for the proportionally low numbers in murine islets but also because available genetic mouse models unavoidably target manipulation

of gene expression in all cell types that make proglucagon, including enteroendocrine L-cells and neurons of the solitary tract nucleus (NTS). Despite this caveat, we were unable to detect evidence that Cre-loxP recombination occurred in L-cells, or that (if it did occur to some degree) it was of any functional consequence. Notably, a previous study showed that serum and gut GLP-1 levels were unchanged following inactivation of the mTOR-associated protein Raptor in proglucagon-expressing cells, in a mouse model that dramatically reduced α cell survival (60) using the same Cre line (41) as this study. Similarly, in a *Gcg*-Cre model targeting profound α cell depletion induced by diphtheria toxin, reporter gene expression was observed in much lower numbers of L-cells compared with islet α cells (61). Together, these data suggest that Cre-mediated recombination targeted to proglucagon-expressing cells is less penetrant in L-cells compared to α cells (possibly from different levels of Cre expression caused by subtle promoter differences); alternatively, perhaps the short lifespan of L-cells lowers the dependence on a functional ERAD system. It is also unlikely that this model has impactful Cre-mediated recombination or ERAD dysfunction in neurons within the NTS or elsewhere in the brain (i.e., as a result of ectopic Cre expression), given the lack of body weight changes or systemic glucose dysregulation as observed with manipulation of proglucagon expression in the CNS (62) and the absence of neurologic dysfunction observed in models of ERAD dysfunction in the brain (31).

Our data show that the effect of ERAD on proPC2 maturation is direct and uncoupled from ER stress, as chemical ER stressors failed to cause the accumulation of proPC2 or the novel truncated proPC2* protein. Instead, proPC2 and proPC2* are SEL1L-HRD1 ERAD substrates that are susceptible to formation of high molecular weight protein aggregates via aberrant disulfide bonds in the absence of ERAD function. The fact that we could detect proPC2* in control α cells after addition MG132 suggests that proPC2* is generated in normal α cells but is quickly degraded by the proteasome, through SEL1L-HRD1 ERAD. Based on the estimated molecular weight of proPC2*, we predict that cleavage of proPC2 within the P domain leads to the generation of the truncated proPC2* protein; however, the specific mechanism producing proPC2* remains unclear. The neuroendocrine protein 7B2 is necessary for formation of an activation-competent proPC2 structure, and in its absence proPC2 is susceptible to misfolding and aggregation in CHO cells (44). However, previous 7B2 structure-function and knockout analyses did not show evidence of proPC2* generation (44, 63, 64). We speculate that the reduction of available 7B2 cofactor in ERAD-deficient α cells exacerbates proPC2 aggregation within the ER, but future studies will be required to clearly define the role of ERAD in the regulation of 7B2 expression and its functional consequences.

Our finding of a new regulator of proPC2 maturation has important therapeutic implications for diabetes and other metabolic diseases, as PC2 acts on a variety of other prohormones, including prosomatostatin, proinsulin, and proopiomelanocortin (POMC). Polymorphisms in the *PCSK2* gene encoding PC2 have been associated with abnormalities in glucose metabolism and risk of type 2 diabetes in specific groups, including African American (65), Chinese (66, 67), and Old Order Amish (68) populations, though the degree of PC2 dysfunction and impact on each of its substrates is less clear. By targeting components of the ERAD pathway, such as SEL1L or HRD1, it may be possible to enhance or inhibit the degradation of proPC2, thereby modulating the levels of mature PC2 and ultimately controlling production of target hormones. Importantly, diminished ERAD activity in our model decreased glucagon production, but not the fraction of glucagon secreted upon stimulation. These data suggest that physiological release of glucagon is proportional to PC2-mediated glucagon production and storage. In α cells, strategies to enhance the function of the ERAD pathway or to stabilize proPC2 in the ER might increase the production of active PC2, leading to higher glucagon levels and improved glucose mobilization during hypoglycemic events. Alternatively, differential processing of proglucagon into glucagon-like peptide 1 (GLP-1) by α cells is a potential mechanism to promote β cell function (69, 70), but whether PC2 contributes to GLP-1 production is not clear (71, 72). Hence, understanding the precise regulatory mechanisms governing proPC2 maturation and function opens new avenues for therapeutic interventions aimed at modulating hormone levels in various metabolic conditions.

In summary, we uncovered a novel function of ERAD in the regulation of proPC2 maturation, which holds significant therapeutic potential. By modulating this system, it may be possible to develop new treatments for diabetes and other metabolic disorders. With the recent identification of human disease-causing variants of SEL1L and HRD1 (31, 73, 74), further research into the ERAD pathway and its interactions with substrates such as proPC2 will be crucial in translating these findings into clinical therapies, ultimately improving outcomes for patients with a range of conditions.

RESEARCH DESIGN AND METHODS

Mice. *Sel1l*$^{fl/fl}$ mice (28) on the C57BL/6J background were crossed with B6;129S-*Gcg*$^{tm1.1(icre)Gkg}$/J (*Gcg*^{iCre}) mice (41) to generate mice with SEL1L deletion in proglucagon-expressing cells (denoted *Sel1L*$^{\Delta Gcg}$ herein), with Cre-negative (*Sel1L*$^{fl/fl}$) or heterozygous (*Sel1L*$^{\Delta Gcg/+}$) littermates used as controls. *Gcg*^{iCre} mice were also crossed with B6.129X1-*Gt(ROSA)26Sor*$^{tm1(EYFP)Cos}$/J reporter mice (Jackson Laboratory 006148). Glucagon-STOP-flox (*Gcg*$^{-/-}$) mice, containing GFP and a poly(A) "stop" signal between exons 2 and 3 of the *Gcg* gene, were previously described (38). Mice were housed in an ambient temperature room with a 12 hr light cycle and fed a normal-chow diet (13% fat, 57% carbohydrate, and 30% protein, LabDiet 5L0D). Males and females were used equally in experiments, except where sexually dimorphic results were observed and reported.

Human islets. Isolated islets from cadaveric donors were obtained from the Human Islet Resource Center at the University of Pennsylvania through the Human Pancreas Analysis Program (75, 76) and Integrated Islet Distribution Program (IIDP) (77), following the guidelines of the Clinical Islet Transplantation Consortium protocol (https://www.isletstudy.org). Briefly, the pancreas was digested following an intraductal injection of collagenase & neutral protease in Hanks' balanced salt solution and then purified on continuous density gradients (Cellgro/Mediatech) using a COBE 2991 centrifuge. Islets were cultured in CIT culture media and maintained in a humidified 5% CO2 incubator. The islets were distributed per the Integrated Islet Distribution Program (IIDP) protocols. After receipt, islets were hand-picked and cultured overnight prior to embedding in low melting point agarose (78) before fixation in 1% paraformaldehyde and mounting in O.C.T. medium in preparation for cryosectioning and immunohistochemistry as previously described (79, 80). Gift of Life, along with other organ procurement organizations, obtained consent from the deceased donors' families for the use of organs in research. All procedures complied with the University of Pennsylvania IRB, Gift of Life leadership team, and UNOS regulations and standards. Donor information is presented in Table S1.

Glucose tolerance tests and in vivo glucagon and GLP-1 secretion. Mice were fasted for 4-6 hr prior to each experiment. Blood was sampled via tail nick. For glucose tolerance testing, blood glucose was measured at baseline prior to intraperitoneal or oral gavage-mediated administration of D-glucose at 1.5 g/kg body weight. Blood glucose was measured 15, 30, 60, and 90 min after glucose administration using a OneTouch Ultra glucometer. For assessment of

glucagon secretion, blood was collected in heparinized tubes before and 30 minutes following intraperitoneal injection of 0.75 units/kg insulin (Novolin R, Fisher Scientific NC0769896). Serum was collected by centrifugation, immediately frozen at -80°C, and thawed prior to measurement by ELISA (Mercodia 10-1281-01). For assessment of total serum GLP-1 levels, mice were given an oral gavage of 3 g/kg D-glucose ten minutes before undergoing isoflurane anesthesia and cardiac puncture. DPPIV inhibitor (Millipore Sigma DPP4) was added to whole blood prior to centrifugation, and serum was frozen at -80°C prior to measurement by ELISA (Crystal Chem 81508).

Pancreatic and gut hormone content. Immediately following sacrifice by cervical dislocation, mouse pancreata were dissected, trimmed of fat, weighed, placed in 3 ml of acid alcohol (1.5% hydrochloric acid in 75% [v/v] ethanol in water) and homogenized for 30 sec. The suspension was rotated for 48 hr at 4°C, centrifuged at 2500 rpm for 30 min at 4°C, then the supernatant stored at -80°C until further analysis. For GLP-1 measurement in gut, the most distal 3 cm of colon was dissected, and gut epithelium was scraped with a coverslip and placed in either acid alcohol or T-PER extraction reagent (Thermo Scientific 78510) with DPPIV inhibitor as previously described (38) for hormone extraction. Glucagon and/or GLP-1 content of diluted supernatant was measured by ELISA, as above. Pancreatic insulin content was measured by ELISA (Crystal Chem 90080).

Histology and islet morphometry. Pancreata were isolated, fixed in 10% neutral buffered formalin (VWR 95042-908) or 4% paraformaldehyde (Electron Microscopy Sciences 15710) for 1.5-16 hours at 4°C. Samples for paraffin embedding and sectioning were dehydrated in 70% ethanol and processed by the University of Michigan Comprehensive Cancer Center Tissue and Molecular Pathology Shared Resource. Alternatively, some pancreata were processed for cryosectioning as previously described (81). Measurements of α- and β-cell mass were performed by the University of Michigan Islet Core. Briefly, five sections per pancreas, each at least 150 μm apart, were labeled with antibodies to insulin (Agilent, Santa Clara, CA) and glucagon (Immunostar, Hudson, WI), then imaged by tiling with a computer-controlled AZ-100 microscope with motorized stage using the NIS Elements AR software (Nikon, Cambridge, MA) and a Coolsnap EZ Digital Camera (Photometrics, Tucson, AZ). After acquisition, α- and β-cell areas were determined by intensity thresholding with manual curation using FIJI 2.14.0. Total α- and β-cell mass were then calculated using the following calculation: [(signal area/total pancreatic section area) x pancreas weight].

Immunofluorescence staining. Deparaffinized tissue sections and cryosections were immunolabeled as described previously (34). The following primary antibodies were used: SEL1L (homemade, (34, 80), 1:200), insulin (Bio-Rad 5330-0104G, 1:500), glucagon (Peninsula Labs/BMA Biomedicals T-5037, 1:200), proglucagon (Cell Signaling Technologies 8233S, 1:200), somatostatin (Abcam ab30788, 1:200), BiP (Abcam 21685, 1:100), OS9 (Abcam ab109510, 1:100), GFP (Abcam 13970, 1:2000), PC2 (Cell Signaling Technologies 14013s, 1:800), proPC2 (homemade, (17), 1:200), GLP-1 (Peninsula Labs/BMA Biomedicals T-4363, 1:200), E-cadherin (BD Biosciences 610181, 1:100). Sections were treated with species-specific secondary antibodies conjugated to Alexa Fluor dyes (Jackson ImmunoResearch; 1:500) followed by mounting with VectaShield (Vector Laboratories, H-1500) or Prolong Gold (Invitrogen P36931) mountant with DAPI. Immunolabeled pancreatic sections were imaged using a Leica DM6000 through the University of Michigan Vision Research Center Morphology and Imaging Core, and Nikon A1 or Leica Stellaris confocal microscopes at the University of Michigan Morphology and Image Analysis Core. Images were prepared for publication using ImageJ software (NIH).

Proliferation and TUNEL assays. Paraffin embedded pancreas sections were immunolabeled with Ki67 (Abcam 15580; 1:100) and glucagon to detect proliferating α cells. TUNEL assay was performed using the In-Situ Cell Death Detection Kit (Roche 11684795910), with glucagon co-labeling by immunofluorescence. Images were acquired using a Leica DM6000 microscope for counting 15-100 islets per mouse to capture a total of 2000-4000 α cells (n = 3-5 per genotype). Cell proliferation and apoptosis rates were calculated as a percentage of Ki67- or TUNEL-positive cells, respectively, per total number of glucagon-positive cells.

Transmission electron microscopy. Whole pancreas was rapidly dissected, placed in fixative (2.5% glutaraldehyde and 4% paraformaldehyde in 0.1 M Na-cacodylate buffer), minced into ~1–2 mm cubes, and fixed overnight at 4°C followed by washes in buffer. Thereafter, samples were submitted to the University of Michigan Microscopy Core for post-fixation in 1% osmium tetroxide, embedding in resin, sectioning, and mounting on grids. Imaging was performed using a JEOL JEM 1400 PLUS microscope.

Islet isolation and secretion. Pancreatic islets were isolated from mice as previously described (82). Briefly, mice were sacrificed by cervical dislocation and pancreata perfused by intraductal injection of 2.5 mL collagenase (Liberase TL [Roche 5401020001] in serum-free

RPMI 1640 [Gibco 11875-085]). Pancreata were incubated at 37°C for ~12 min with an additional 1 mL of digestion solution. Digestion was stopped by adding cold HBSS with 10% FBS. Islets were washed and hand-picked under a dissecting microscope, then allowed to recover overnight in RPMI medium in a humidified incubator (95% air, 5% CO_2) at 37°C prior to further analysis. For static secretion experiments, 10 size-matched purified islets were incubated in 200 µl KRBB (Krebs-Ringer Solution, HEPES-buffered, Thermo-Fisher Scientific J67795.K2) containing D-glucose +/- L-arginine hydrochloride (MilliporeSigma A5131) and media collected at the indicated times. Following the experiments, islets were lysed (50 mM Tris HCl pH 7.4, 1 mM EDTA, protease inhibitor [MilliporeSigma P8340], phosphatase inhibitor [MilliporeSigma P5726]), total protein concentrations determined by Pierce BCA assay (Thermo Fisher Scientific), and media and lysate glucagon levels measured by ELISA as above.

Cell culture and Western blotting. Control αTC(1-6) cells were a kind gift from Ernesto Bernal-Mizrachi and also independently obtained from ATCC (CRL-2934). Cells were cultured in αTC complete medium per manufacturer recommendations. CRISPR-targeting sgRNA oligonucleotides designed against mouse *Sel1L*, *Hrd1*, or *Pcsk2* (sequences listed in Supplemental Table S2) were inserted into the lentiCRISPR, version 2 vector (Addgene, 52961) prior to transfection in αTC (or HEK293T) cells and puromycin selection of modified cells as previously described (74). Cells transfected with the empty lentiCRISPR vector were used as a control. In some experiments, cells were treated with 50 µg/ml cycloheximide (Sigma-Aldrich C7698). Upon experiment completion, cells were lysed in NP-40 lysis buffer (50 mM Tris HCl at pH 7.5, 150 mM NaCl, 1% NP-40, 1 mM EDTA) with protease inhibitor, DTT (MilliporeSigma, 1 mM), and phosphatase inhibitor cocktail. Lysates were incubated on ice for 30 min and centrifuged at 16,000 g for 10 min. Supernatants were collected and protein concentrations determined using Bradford assay (Bio-Rad). For reducing SDS-PAGE analysis, proteins were heat-denatured at 65-90°C for 10 min in 5x SDS sample buffer (250 mM Tris-HCl pH 6.8, 10% sodium dodecyl sulfate, 0.05% bromophenol blue, 50% glycerol, and 1.44 M β-mercaptoethanol). For non-reducing conditions, lysates were prepared at 37°C with 5x non-denaturing sample buffer (250 mM Tris-HCl pH 6.8, 1% sodium dodecyl sulfate, 0.05% bromophenol blue, 50% glycerol) for 60 min (31). Samples were resolved by gel electrophoresis, then transferred to PVDF membranes (Bio-Rad). Some membranes were fixed with PBS containing 4% paraformaldehyde and 0.01% glutaraldehyde for 30 min (83). Membranes were blocked with 5% milk in Tris-buffered saline Tween-20 (TBST) for 30 min, then incubated overnight at 4°C with antibodies prepared in 2% bovine serum albumin (BSA) in

TBST. The following primary antibodies were used: anti-SEL1L (homemade, Shrestha JCI 2020, 1:10,000), anti-HRD1 (Proteintech 13473-1, 1:2,000), anti-OS9 (Abcam ab109510, 1:5,000), anti-BiP (Abcam ab21685, 1:5,000), anti-IRE1α (Cell Signaling Technologies [CST] 3294, 1:2,000), anti-PERK (CST 3192, 1:1000), anti-eIF2α (CST 9722, 1:1000), anti-phospho-eIF2α (CST 9721, 1:1000), anti-PC2 (CST 14013s, 1:500), anti-PC2 C-terminus (homemade, (45), 1:200), anti-proPC2 ((17), 1:200), anti-7B2 (homemade, (63), 1:200), and anti-HSP90 (Abcam ab13492; 1:2000). Membranes were washed and then incubated with goat anti-rabbit or anti-mouse IgG-HRP (Bio-Rad 1706515 and 1706516, 1:3000-1:5000) in 5% milk in TBST for 1 hr at room temperature, washed, and labeled with Clarity ECL substrate (Bio-Rad). Blots were imaged with a Bio-Rad ChemiDoc and protein band intensity was quantified using Image Lab software (Bio-Rad).

Immunoprecipitation and ubiquitination assay. Assay was performed as previously described (73). Briefly, control and ΔHrd1 αTC cells were treated with 10 μM MG132 (Enzo, BML-PI102) for 2 hr. Whole cell lysates were prepared in non-reducing lysis buffer as above. The supernatant was denatured with 1% SDS and 5 mM DTT at 95°C for 10 min, then diluted 1:10 with NP-40 lysis buffer and mixed with control IgG antibody (Cell Signaling Technologies 2729) or anti-proPC2 antibody (as above). This mixture was incubated with 15 μl anti-protein A agarose (Millipore Sigma, 11719408001) overnight at 4°C with gentle rocking. Agarose beads were washed three times with NP-40 lysis buffer and eluted in the SDS sample buffer at 95°C for 5 min, followed by SDS-PAGE and Western blotting as above.

PC2 enzyme assay. A substrate-specific PC2 assay was performed as previously described (46). Control, ΔSel1L, and ΔHrd1 αTC cells were washed and sonicated in ice-cold lysis buffer (0.1 M sodium acetate, pH 5.5, 1% Triton X-100, 50 μM trans-epoxysuccinyl-L-leucylamido[4-guanidino]butane [E-64], 50 uM pepstatin, 1 mM phenylmethylsulfonyl fluoride [PMSF]) and centrifuged at 10,000g at 4°C for 10 minutes. The supernatant was transferred to clean microcentrifuge tubes and protein concentrations determined using a Bradford assay (Bio-Rad). Samples of equal protein concentration (10 μg) were added to a polypropylene microtiter plate with 40 μl reaction buffer mix (2 mM $CaCl_2$, 0.1 M sodium acetate buffer [pH 5.0], 0.1% Triton X-100, 5.6 mM Nα-tosyl-L-lysine chloromethyl ketone hydrochloride [TLCK], 6 mM N-p-tosyl-L-phenylalanine chloromethyl ketone [TPCK], 2 mM E-64, 2 mM pepstatin). Each assay was performed in duplicate, both with and without the synthetic 7B2 C-terminal peptide (7B2-CT). The reaction was preincubated for 15 min at 37°C, followed by addition of 5 μl of substrate, pGlu-Arg-Thr-Lys-Arg-MCA (RTKR-MCA, final concentration 0.2 mM in dimethyl sulfoxide

[DMSO]). The reaction mixture was briefly mixed and the fluorescence of the liberated aminomethyl-coumarin (AMC; excitation 380 nm, emission 460 nm) was documented every two minutes using a fluorometer.

RNA extraction, microarray, cDNA synthesis and qPCR analysis. RNA was isolated by phenol extraction and concentration determined using a NanoDrop 2000 UV-Vis Spectrophotometer. RT-PCR for assessment of *Xbp1* mRNA splicing and qPCR analyses were performed as previously described (84). All PCR data were normalized to the ribosomal *L32* or *Rplp0* gene expression level. All qPCR primer sequences are shown in Supplemental Table S3.

Protein structure analysis. Protein structures were predicted using the AlphaFold 3 server, located at https://alphafoldserver.com/ (85). Images were rendered with PyMOL (version 2.3.2).

Statistical analysis. Results are expressed as mean ± SEM unless otherwise stated. Statistical analyses were performed in GraphPad Prism (GraphPad Software Inc.). Comparisons between two groups were made by unpaired two-tailed Student's t test. Comparisons between multiple groups were made by one- or two-way ANOVA followed by Šidák or Tukey post-test, as noted. *P* values less than 0.05 were considered statistically significant. All experiments were repeated at least twice, or performed with several independent biological samples, with representative data shown.

Study approval. All animal procedures were approved by and done in accordance with the IACUC at the University of Michigan Medical School (PRO00008989/PRO00010658/PRO00011495).

Data availability. The materials and reagents used are either commercially available or are available upon request. All data and materials for the manuscript are described in Methods. Values for all datapoints in graphs are reported in the Supporting Data Values file.

AUTHOR CONTRIBUTIONS

W.Z., L.P., X.C., A.C.R., R.R., B.P., X.W., L.L., H.H., B.G., and R.B.R. performed experiments that were designed by W.Z., L.P., L.Q., and R.B.R; N.S. made the initial crosses of knockout mice and provided experimental support and helpful discussion; C.L., A.N., P.A., D.S., and I.L. provided key reagents and helpful discussion; L.Q. and R.B.R. supervised the project and wrote the manuscript. All other authors edited and approved the manuscript.

ACKNOWLEDGMENTS

We thank Dr. Ernesto Bernal-Mizrachi for sharing αTC(1-6) cells; Dr. Yewei Ji, Dr. Mauricio Torres, Dr. Leena Haataja, Jianing Zhang, Elise Corden, and Steve Lentz for experimental support; and all other members of the Qi and Arvan laboratories for comments and technical assistance. This work was completed with the assistance of NIH-supported core facilities, including the Microscopy, Imaging and Cellular Physiology Core (MICPC) and Islet Isolation Laboratory supported by the National Institute for Diabetes, Digestive, and Kidney (NIDDK)-funded Michigan Diabetes Research Center (P30DK020572 and Shared Instrument Grant S10OD28612-01-A1), the University of Michigan Vision Research Center Morphology and Imaging Core supported by the National Eye Institute (P30EY007003), the Tissue and Molecular Pathology Shared Resource supported by the National Cancer Institute (P30CA04659229), and the University of Michigan Biomedical Research Core Facilities Microscopy Core. This manuscript used human islets acquired from the University of Pennsylvania Islet Transplant Center in collaboration with the Human Pancreas Analysis Program (HPAP-RRID:SCR_016202), a Human Islet Research Network (RRID:SCR_014393) consortium (UC4DK112217), and the Integrated Islet Distribution Program (IIDP) (RRID:SCR_014387) through City of Hope (UC4DK098085), supported by Beckman Research Center grant 10028044 (to A.N.). We thank the human islet donors and their families for their generous contribution. This work was supported by R24DK110973 (to P.A.), R01DK11174 and 2-SRA-2018-539-A-B (to P.A. and L.Q.), R01DK121995 (to D.A.S), R01DK137794 and R35GM130292 (to L.Q.), and 5T32DK007245 and K08DK129719 (to R.B.R.).

FIGURE LEGENDS

Figure 1. The endoplasmic reticulum (ER) is a prominent feature of normal and proliferative islet α cells. A, Transmission electron microscopy (TEM) image of a normal α cell (yellow dashed outline), demonstrating prominent stacks of rough ER. Adjacent β and δ cells are labeled. Scale bar of left panel, 1 μm; of inset, 600 nm. B, TEM images showing prominent ER stacks (asterisks) in highly proliferative α cells from *Gcg*$^{-/-}$ mice compared to littermate controls. Scale bars, 1 μm. Additional TEM images are shown in Figure S1A. C, Representative islets from *Gcg*$^{-/-}$ mice and littermate controls, immunolabeled for the ER chaperone BiP and either glucagon (GCG, top panels) or insulin (INS, bottom panels). D, Violin plot shows the distribution of relative BiP immunofluorescence in islets from *Gcg*$^{-/-}$ and control mice, quantified as the ratio of the average BiP intensity of non-β cells to β cells. Data represents a total of 37-61 islets from n = 3-4 mice per genotype, with median line shown in white and quartile lines in black. ***P < 0.001, unpaired two-tailed Student's t test. E, Representative islet cryosections immunolabeled for the ER-associated degradation (ERAD) component SEL1L and either glucagon (GCG, top panels) or GFP (as expressed by the construct inserted into the Gcg gene, bottom panels). White arrows mark examples of α cells. Yellow arrows denote peripheral non-α islet cells that highly express SEL1L, notably with absence of glucagon expression. F, Violin plot shows the distribution of SEL1L immunofluorescence in GCG+ or GFP+ α cells, normalized to the mean intensity of SEL1L in β cells within the same islet. Data represents a total of 1400-2300 α cells from n = 3-4 mice per genotype, with median line shown in white and quartile lines in black. ***P < 0.001, unpaired two-tailed Student's t test. G, Cryosections of isolated islets from human islet donors immunolabeled for SEL1L and glucagon (GCG). The islet in the top panels is from a donor without diabetes (No DM), and the islet in the bottom panels is from a donor with a two-year history of type 2 diabetes (T2DM); see Table S1 for further donor characteristics. Scale bar for left panels in C-E, 50 μm.

Figure 2. Inactivation of SEL1L-HRD1 ERAD disrupts ER homeostasis in α cells but does not lead to accumulation of proglucagon-derived peptides. Representative islets from adult (4-8 month-old) *Sel1L*$^{\Delta Gcg}$ mice and *Sel1L*$^{fl/fl}$ littermate controls, immunolabeled for glucagon and the ERAD component SEL1L (A), the ERAD cofactor/substrate OS9 (B), the ER chaperone BiP (C), or proglucagon (D). Scale bars of left panels, 50 μm. Violin plots show the distribution of immunofluorescence intensity of BiP, proglucagon, or glucagon in 500-1300 α cells from n = 3-4 mice per genotype, with median line shown in white and quartile lines in black. ***P < 0.001, unpaired two-tailed Student's t test.

Figure 3. ERAD inactivation in α cells does not affect systemic growth or glucose tolerance but limits glucagon production with age. A-B, Body weight and oral glucose tolerance (OGTT) in adult (4-8 month-old) male and female *Sel1L*$^{\Delta Gcg}$ mice (red triangles) and *Sel1L*$^{fl/fl}$ controls (gray circles). Each data point represents $n > 6$ mice, shown as mean ± SEM. C, Serum glucagon and glucose levels *in vivo* in adult male (>4 months) and female (>8 months) *Sel1L*$^{\Delta Gcg}$ mice (red triangles) and *Sel1L*$^{fl/fl}$ controls (gray circles) in response to insulin-induced hypoglycemia. For serum glucagon, each data point represents data from one mouse, with mean ± SEM bars shown; for blood glucose, data represents mean ± SEM. D, Acid ethanol-extracted pancreatic glucagon content in adult (4-8 month-old) mice. Each data point represents data from one mouse, with mean ± SEM shown. E, Normalized glucagon secretion and total islet glucagon content from isolated *Sel1L*$^{\Delta Gcg}$ and *Sel1L*$^{fl/fl}$ islets. Each data point represents data from one mouse, with mean ± SEM shown. F, Representative transmission electron microscopy images of α cells from adult *Sel1L*$^{\Delta Gcg}$ mice and *Sel1L*$^{fl/fl}$ controls, with ER stacks or dilated ER lumen denoted by asterisks. Scale bar, 600 nm. $^{*}P < 0.05$, $^{**}P < 0.01$, $^{***}P < 0.001$; *NS*, not significant with $P > 0.05$; a two-way ANOVA with Šidák post-test was performed for serum glucagon tests in C, and an unpaired two-tailed Student's t test was performed to compare groups in all other graphs.

Figure 4. Inactivation of SEL1L-HRD1 ERAD in α cells leads to accumulation of prohormone convertase 2 in vivo. A, Schematic diagram of the mouse preproPC2 protein, denoting the locations of antibody targets. SP, signal peptide; Pro, propeptide; CT, C-terminal region. B, AlphaFold 3 structural model of the mouse proPC2 protein. C-D, Representative islets from *Sel1L*$^{\Delta Gcg}$ mice and *Sel1L*$^{fl/fl}$ controls, immunolabeled for the PC2 proprotein (C) or total prohormone convertase 2 (PC2 CST, D). Scale bars, 25 μm. Violin plots at right show the distribution of immunofluorescence intensity of (pro)PC2 in glucagon+ cells from 800-1300 cells with $n = 3$-4 mice per genotype, with median line shown in white and quartile lines in black. $^{***}P < 0.001$; unpaired two-tailed Student's t test.

Figure 5. Inactivation of SEL1L-HRD1 ERAD in α cells alters processing of prohormone convertase 2. A, Western blot of SEL1L and HRD1 expression in αTC1-6 cells following CRISPR-mediated deletion of Sel1L (ΔSel1L) or Hrd1 (ΔHrd1) compared to vector-treated controls (αTC). B-D, Western blots of αTC cells using antibodies to the PC2 proprotein (B), PC2 catalytic domain (C), or PC2 C-terminal domain (D), with band quantification shown at right.

Note the generation of an N-terminal fragment of the proPC2 protein in ΔSel1L and ΔHrd1 cells, denoted proPC2*. E-F, Western blot of αTC cells following CRISPR-mediated deletion of SEL1L (ΔSel1L), HRD1 (ΔHrd1), and/or PC2 (ΔPC2), labeled with antibodies to the catalytic domain of PC2 (E) or to the PC2 proprotein (F). G, Western blot of tunicamycin (Tm)- and thapsigargin (Tg)-treated control αTC cells, labeled with an antibody to proPC2, with band quantification shown at right. H, Quantitative RT-PCR of the *Pcsk2* gene encoding PC2 in αTC cells. In bar graphs, each data point represents a single technical replicate from 2-3 independent experiments, shown as mean ± SEM. *$P < 0.05$; **$P < 0.01$; ***$P < 0.001$; *NS*, not significant ($P > 0.05$); one-way ANOVA with Šidák post-test.

Figure 6. Inactivation of SEL1L-HRD1 ERAD in α cells alters processing of prohormone convertase 2. A-B, Western blot of αTC cells following 0, 3, and 6 hours of treatment with cycloheximide (CHX) to inhibit new protein synthesis, labeled with antibodies targeting the catalytic domain of PC2 (CST, A) or proPC2 (B). Quantification of the relative expression of each (pro)PC2 form over time is shown at right (data points are averages of $n = 2$ technical replicates from three independent experiments, shown as mean ± SEM). C, Western blot of αTC cell lysates prepared under reducing and nonreducing conditions, labeled with antibodies to proPC2. Note that images from reducing and nonreducing conditions are from the same blot, cropped for clarity. D, Western blot analysis of protein ubiquitination before (Input, left) and after (Denaturing IP, right) immunoprecipitation with antibodies to proPC2 or IgG control in αTC and ΔHrd1 cells. E, Western blot and quantification of the proPC2 chaperone protein 7B2 in αTC, ΔSel1L, and ΔHrd1 cells. Each data point represents a single technical replicate, shown as mean ± SEM. F, PC2 enzymatic activity of cell lysates as measured by a substrate-specific aminomethylcoumarin assay, performed with and without the addition of exogenous 7B2 C-terminal (CT) peptide as a specific PC2 inhibitor. In the time course graph, each data point represents the mean ± SEM of six technical replicates from two independent experiments. In the bar graph, each data point represents the rate of change in fluorescence intensity for individual replicates in the time course graph, shown as mean ± SEM. For each graph, *$P < 0.05$; **$P < 0.01$; ***$P < 0.001$; *NS*, not significant ($P > 0.05$); two-way ANOVA with Tukey post-test was performed in A-B and one-way ANOVA with Šidák post-test was performed in E-F.

Figure 7. Working model. A, SEL1L-HRD1 ERAD is a critical ER protein quality control pathway in α cells, targeting misfolded and/or aggregated pro-prohormone convertase 2 (proPC2) and aberrantly cleaved proPC2* molecules for proteasomal degradation. SEL1L-

HRD1 ERAD function is essential to allow for packaging of properly folded proPC2 and proglucagon into secretory granules, where proPC2 is then activated into the functional PC2 enzyme that cleaves proglucagon into glucagon - thus promoting α cell function. B, Defective SEL1L-HRD1 ERAD function in α cells leads to aggregation of proPC2 and aberrantly cleaved proPC2*, limiting the packaging of activation-competent proPC2 into secretory granules and thus limiting the production of mature glucagon.

SUPPLEMENTAL FIGURE LEGENDS

Figure S1. The endoplasmic reticulum (ER) is a prominent feature of normal and proliferative α cells. A, Rough ER (asterisks) in α cells (yellow dashed lines) from *Gcg*$^{-/-}$ mice and littermate controls. Scale bars, 1 μm. B, Representative islets from *Gcg*$^{-/-}$ mice and controls, immunolabeled for somatostatin (SST; labeling islet δ cells) and proglucagon (proGCG), glucagon (GCG), or GLP-1. Islet borders are outlined. Scale bars, 50 μm.

Figure S2. *Gcg*^{iCre} mice show effective recombination in islet α cells but not intestinal L-cells. A, Colon from *Sel1L*$^{\Delta Gcg}$ mice and *Sel1L*$^{fl/fl}$ littermate controls, immunolabeled with antibodies to glucagon and BiP. B, Representative section from pancreas and colon from control mice immunolabeled with antibodies to glucagon and GLP-1, along with E-cadherin in the colon sample. Note the similarities in labeling suggest that both antibodies also bind to the full-length proglucagon protein. C, Representative islets from *R26R-EYFP*$^{\Delta Gcg/+}$ (Cre +) mice and *R26R-EYFP*$^{fl/+}$ (Cre -) controls, immunolabeled with antibodies to glucagon and GFP; quantification of GFP+ α cells is shown in C' with each data point representing one islet. D, Intestinal cryosections from *R26R-EYFP*$^{\Delta Gcg/+}$ mice and Cre-negative *R26R-EYFP*$^{fl/+}$ controls, immunolabeled with antibodies to (pro)glucagon and GFP. Scale bars, 50 μm. E, Pancreatic glucagon content in *R26R-EYFP*$^{\Delta Gcg/+}$ (Cre +) mice and *R26R-EYFP*$^{fl/+}$ (Cre -) controls at 6-13 weeks of age, mixed sexes. Each data point represents one mouse. F, Plasma total GLP-1 (1-26, 7-36, and 9-36) levels following glucose administration in male and female *Sel1L*$^{\Delta Gcg}$ mice and *Sel1L*$^{fl/fl}$ controls. G, Total GLP-1 extracted from distal colon epithelium in male *Sel1L*$^{\Delta Gcg}$ mice and *Sel1L*$^{fl/fl}$ controls. For F-G, each data point represents one mouse. *NS*, not significant ($P > 0.05$), unpaired two-tailed Student's t test. Data represent mean ± SEM.

Figure S3. SEL1L inactivation in pancreatic α cells disrupts ER morphology and glucagon production but does not affect β cell morphology or function. A, Transmission

electron microscopy (TEM) of pancreatic islets from an aged *Sel1L*$^{\Delta Gcg}$ mouse and littermate control. B, TEM of representative β cells from each genotype. Scale bars in A-B, 1 μm. C, Acid-alcohol extracted pancreatic insulin content in male and female *Sel1L*$^{\Delta Gcg}$ mice and *Sel1L*$^{fl/fl}$ controls. D-F, Alpha cell mass (D), TUNEL labeling for α cell apoptosis (E), and Ki67+ α cell proliferation (F) in adult (4-8 month-old) *Sel1L*$^{\Delta Gcg}$ mice and *Sel1L*$^{fl/fl}$ controls. In graphs, each point represents data from one mouse, shown as mean ± SEM. **P* < 0.05, *NS*, not significant with *P* > 0.05; unpaired two-tailed Student's t test.

Figure S4. Inactivation of SEL1L or HRD1 in αTC cells leads to mild activation of the unfolded protein response in vitro. A, Immunofluorescence of αTC1-6 cells following CRISPR-mediated deletion of Sel1L (ΔSel1L) or Hrd1 (ΔHrd1) compared to vector-treated controls, labeled for Sel1L and the ER marker KDEL. Note that deletion of Sel1L was incomplete, so Hrd1 deletion was used as an alternative means to inactivate ERAD function. Scale bar, 50 μm. B-C, Quantification of SEL1L (B) and HRD1 (C) protein expression in αTC1-6 cells following CRISPR-mediated deletion of SEL1L (ΔSel1L, light gray/triangles) or HRD1 (ΔHrd1, dark gray/squares) compared to vector-treated αTC controls (white/circles). Representative Western blots are shown in Fig. 4D. D-F, Western blots and quantification of ERAD substrate and UPR sensor IRE1α, and ERAD substrate OS9, in αTC cells with targeted deletion of SEL1L or HRD1. Note that the HSP90 loading control is identical to that shown in Fig. 4D. G-J, Western blots and quantification of UPR sensor PERK and its downstream effector eIF2α (P, phosphorylated; T, total) in αTC cells with targeted deletion of SEL1L or HRD1. Western blot experiments were performed at least three times, with each data point in graphs representing individual technical replicates and summary bars shown as mean ± SEM, expressed as arbitrary units (a.u.). K, RT-PCR detection of *Xbp1* mRNA in unspliced (Xbp1u) and spliced (Xbp1s) forms. Quantification was calculated as the ratio of Xbp1s to total Xbp1 (*n* = 1-3 x 5 experiments), with each data point in graph representing individual technical replicates and summary bars shown as mean ± SEM. Tunicamycin (Tm) treatment was used as a positive control for activation of IRE1α-mediated Xbp1 splicing; the "αTC + Tm" group is an aggregate of Tm-treated replicates from each genotype. **P* < 0.05, ***P* < 0.01, ****P* < 0.001, *NS*, not significant (*P* > 0.05); one-way ANOVA with Šidák post-test.

REFERENCES

1. Unger RH, and Cherrington AD. Glucagonocentric restructuring of diabetes: a pathophysiologic and therapeutic makeover. *J Clin Invest.* 2012;122(1):4 - 12.
2. Finan B, Capozzi ME, and Campbell JE. Repositioning Glucagon Action in the Physiology and Pharmacology of Diabetes. *Diabetes.* 2020;69(4):532-41.
3. Brooks EP, and Sussel L. Not the second fiddle: alpha cell development, identity, and function in health and diabetes. *J Endocrinol.* 2023;258(2).
4. Unger RH, and Orci L. Physiology and pathophysiology of glucagon. *Physiological Reviews.* 1976;56(4):778 - 826.
5. Dinneen S, Alzaid A, Turk D, and Rizza R. Failure of glucagon suppression contributes to postprandial hyperglycaemia in IDDM. *Diabetologia.* 1995;38(3):337 - 43.
6. Pearson MJ, Unger RH, and Holland WL. Clinical Trials, Triumphs, and Tribulations of Glucagon Receptor Antagonists. *Diabetes Care.* 2016;39(7):1075 - 7.
7. Pettus J, Reeds D, Cavaiola TS, Boeder S, Levin M, Tobin G, et al. Effect of a glucagon receptor antibody (REMD-477) in type 1 diabetes: A randomized controlled trial. *Diabetes Obes Metab.* 2018;20(5):1302-5.
8. Pettus J, Boeder SC, Christiansen MP, Denham DS, Bailey TS, Akturk HK, et al. Glucagon receptor antagonist volagidemab in type 1 diabetes: a 12-week, randomized, double-blind, phase 2 trial. *Nat Med.* 2022;28(10):2092-9.
9. Wei R, Gu L, Yang J, Yang K, Liu J, Le Y, et al. Antagonistic Glucagon Receptor Antibody Promotes α-Cell Proliferation and Increases β-Cell Mass in Diabetic Mice. *Iscience.* 2019;16:326 - 39.
10. Hayashi Y, Yamamoto M, Mizoguchi H, Watanabe C, Ito R, Yamamoto S, et al. Mice deficient for glucagon gene-derived peptides display normoglycemia and hyperplasia of islet {alpha}-cells but not of intestinal L-cells. *Mol Endocrinol.* 2009;23(12):1990 - 9.
11. Gelling RW, Du XQ, Dichmann DS, Romer J, Huang H, Cui L, et al. Lower blood glucose, hyperglucagonemia, and pancreatic alpha cell hyperplasia in glucagon receptor knockout mice. *Proc Natl Acad Sci USA.* 2003;100(3):1438 - 43.
12. Svendsen B, Larsen O, Gabe MBN, Christiansen CB, Rosenkilde MM, Drucker DJ, et al. Insulin Secretion Depends on Intra-islet Glucagon Signaling. *CellReports.* 2018;25(5):1127 - 34.e2.
13. Capozzi ME, Svendsen B, Encisco SE, Lewandowski SL, Martin MD, Lin H, et al. β Cell tone is defined by proglucagon peptides through cAMP signaling. *JCI Insight.* 2019;4(5):66.
14. Capozzi ME, Wait JB, Koech J, Gordon AN, Coch RW, Svendsen B, et al. Glucagon lowers glycemia when beta-cells are active. *JCI Insight.* 2019;5(16).
15. El K, Capozzi ME, and Campbell JE. Repositioning the Alpha Cell in Postprandial Metabolism. *Endocrinology.* 2020;161(11).

16. Sandoval DA, and D'Alessio DA. Physiology of proglucagon peptides: role of glucagon and GLP-1 in health and disease. *Physiological Reviews.* 2015;95(2):513 - 48.
17. Muller L, Cameron A, Fortenberry Y, Apletalina EV, and Lindberg I. Processing and sorting of the prohormone convertase 2 propeptide. *The Journal of biological chemistry.* 2000;275(50):39213 - 22.
18. Lamango NS, Apletalina E, Liu J, and Lindberg I. The proteolytic maturation of prohormone convertase 2 (PC2) is a pH-driven process. *Arch Biochem Biophys.* 1999;362(2):275-82.
19. Riahi Y, Israeli T, Cerasi E, and Leibowitz G. Effects of proinsulin misfolding on β-cell dynamics, differentiation and function in diabetes. *Diabetes Obes Metab.* 2018;20 Suppl 2:95 - 103.
20. Sokolowski EK, Kursawe R, Selvam V, Bhuiyan RM, Thibodeau A, Zhao C, et al. Multi-omic human pancreatic islet endoplasmic reticulum and cytokine stress response mapping provides type 2 diabetes genetic insights. *Cell Metab.* 2024;36(11):2468-88 e7.
21. Eizirik DL, Cardozo AK, and Cnop M. The role for endoplasmic reticulum stress in diabetes mellitus. *Endocrine Reviews.* 2008;29(1):42 - 61.
22. Shrestha N, Franco ED, Arvan P, and Cnop M. Pathological β-Cell Endoplasmic Reticulum Stress in Type 2 Diabetes: Current Evidence. *Frontiers in endocrinology.* 2021;12:650158.
23. Shrestha N, Reinert RB, and Qi L. Endoplasmic Reticulum Protein Quality Control in β Cells. *Seminars in cell & developmental biology.* 2020;103:59 - 67.
24. Christianson JC, Jarosch E, and Sommer T. Mechanisms of substrate processing during ER-associated protein degradation. *Nat Rev Mol Cell Biol.* 2023;24(11):777-96.
25. Krshnan L, van de Weijer ML, and Carvalho P. Endoplasmic Reticulum-Associated Protein Degradation. *Cold Spring Harb Perspect Biol.* 2022;14(12).
26. Qi L, Tsai B, and Arvan P. New Insights into the Physiological Role of Endoplasmic Reticulum-Associated Degradation. *Trends in cell biology.* 2017;27(6):430 - 40.
27. Hwang J, and Qi L. Quality Control in the Endoplasmic Reticulum: Crosstalk between ERAD and UPR pathways. *Trends in Biochemical Sciences.* 2018;43(8):593-605.
28. Sun S, Shi G, Han X, Francisco AB, Ji Y, Mendonça N, et al. Sel1L is indispensable for mammalian endoplasmic reticulum-associated degradation, endoplasmic reticulum homeostasis, and survival. *Proceedings of the National Academy of Sciences.* 2014;111(5):E582 - 91.
29. Gardner RG, Swarbrick GM, Bays NW, Cronin SR, Wilhovsky S, Seelig L, et al. Endoplasmic reticulum degradation requires lumen to cytosol signaling. Transmembrane control of Hrd1p by Hrd3p. *J Cell Biol.* 2000;151(1):69-82.
30. Lilley BN, and Ploegh HL. Multiprotein complexes that link dislocation, ubiquitination, and extraction of misfolded proteins from the endoplasmic reticulum membrane. *Proc Natl Acad Sci U S A.* 2005;102(40):14296-301.
31. Lin LL, Wang HH, Pederson B, Wei X, Torres M, Lu Y, et al. SEL1L-HRD1 interaction is required to form a functional HRD1 ERAD complex. *Nature Communications.* 2024;15(1):1440.

32. Shi G, Somlo D, Kim GH, Prescianotto-Baschong C, Sun S, Beuret N, et al. ER-associated degradation is required for vasopressin prohormone processing and systemic water homeostasis. *J Clin Invest.* 2017;127(10):556 - 64.
33. Kim GH, Shi G, Somlo DR, Haataja L, Song S, Long Q, et al. Hypothalamic ER-associated degradation regulates POMC maturation, feeding, and age-associated obesity. *J Clin Invest.* 2018;128(3).
34. Shrestha N, Liu T, Ji Y, Reinert RB, Torres M, Li X, et al. Sel1L-Hrd1 ER-associated degradation maintains β cell identity via TGF-β signaling. *J Clin Invest.* 2020;130(7):3499 - 510.
35. Shrestha N, Torres M, Zhang J, Lu Y, Haataja L, Reinert RB, et al. Integration of ER protein quality control mechanisms defines beta cell function and ER architecture. *J Clin Invest.* 2023;133(1):e163584.
36. Hu Y, Gao Y, Zhang M, Deng KY, Singh R, Tian Q, et al. Endoplasmic Reticulum-Associated Degradation (ERAD) Has a Critical Role in Supporting Glucose-Stimulated Insulin Secretion in Pancreatic beta-Cells. *Diabetes.* 2019;68(4):733-46.
37. Wu T, Zhang S, Xu J, Zhang Y, Sun T, Shao Y, et al. HRD1, an Important Player in Pancreatic beta-Cell Failure and Therapeutic Target for Type 2 Diabetic Mice. *Diabetes.* 2020;69(5):940-53.
38. Chambers AP, Sorrell JE, Haller A, Roelofs K, Hutch CR, Kim K-S, et al. The Role of Pancreatic Preproglucagon in Glucose Homeostasis in Mice. *Cell Metabolism.* 2017;25(4):927 - 34.e3.
39. Dean ED, Li M, Prasad N, Wisniewski SN, Deylen AV, Spaeth J, et al. Interrupted Glucagon Signaling Reveals Hepatic α Cell Axis and Role for L-Glutamine in α Cell Proliferation. *Cell Metabolism.* 2017;25(6):1362 - 73.e5.
40. Kim J, Okamoto H, Huang Z, Anguiano G, Chen S, Liu Q, et al. Amino Acid Transporter Slc38a5 Controls Glucagon Receptor Inhibition-Induced Pancreatic α Cell Hyperplasia in Mice. *Cell Metabolism.* 2017;25(6):1348 - 61.e8.
41. Shiota C, Prasadan K, Guo P, Fusco J, Xiao X, and Gittes GK. Gcg (CreERT2) knockin mice as a tool for genetic manipulation in pancreatic alpha cells. *Diabetologia.* 2017;13(Suppl 1):126 - 10.
42. Srinivas S, Watanabe T, Lin CS, William CM, Tanabe Y, Jessell TM, et al. Cre reporter strains produced by targeted insertion of EYFP and ECFP into the ROSA26 locus. *BMC Dev Biol.* 2001;1:4.
43. Furuta M, Yano H, Zhou A, Rouillé Y, Holst JJ, Carroll R, et al. Defective prohormone processing and altered pancreatic islet morphology in mice lacking active SPC2. *Proceedings of the National Academy of Sciences.* 1997;94(13):6646-51.
44. Lee S-N, and Lindberg I. 7B2 prevents unfolding and aggregation of prohormone convertase 2. *Endocrinology.* 2008;149(8):4116-27.
45. Muller L, Zhu X, and Lindberg I. Mechanism of the Facilitation of PC2 Maturation by 7B2: Involvement in ProPC2 Transport and Activation but Not Folding. *The Journal of Cell Biology.* 1997;139(3):625-38.

46. Li Q-L, Naqvi S, Shen X, Liu Y-J, Lindberg I, and Friedman TC. Prohormone convertase 2 enzymatic activity and its regulation in neuro-endocrine cells and tissues. *Regulatory Peptides.* 2003;110(3):197-205.
47. Zuber C, Fan J-Y, Guhl B, and Roth J. Misfolded proinsulin accumulates in expanded pre-Golgi intermediates and endoplasmic reticulum subdomains in pancreatic beta cells of Akita mice. *FASEB J.* 2004;18(7):917 - 9.
48. Marchetti P, Bugliani M, Lupi R, Marselli L, Masini M, Boggi U, et al. The endoplasmic reticulum in pancreatic beta cells of type 2 diabetes patients. *Diabetologia.* 2007;50(12):2486 - 94.
49. Jacquemyn J, Cascalho A, and Goodchild RE. The ins and outs of endoplasmic reticulum-controlled lipid biosynthesis. *EMBO Rep.* 2017;18(11):1905-21.
50. Longuet C, Robledo AM, Dean ED, Dai C, Ali S, McGuinness I, et al. Liver-specific disruption of the murine glucagon receptor produces α-cell hyperplasia: evidence for a circulating α-cell growth factor. *Diabetes.* 2013;62(4):1196 - 205.
51. Larger E, Wewer Albrechtsen NJ, Hansen LH, Gelling RW, Capeau J, Deacon CF, et al. Pancreatic alpha-cell hyperplasia and hyperglucagonemia due to a glucagon receptor splice mutation. *Endocrinol Diabetes Metab Case Rep.* 2016;2016:16-0081.
52. Kazda CM, Ding Y, Kelly RP, Garhyan P, Shi C, Lim CN, et al. Evaluation of Efficacy and Safety of the Glucagon Receptor Antagonist LY2409021 in Patients With Type 2 Diabetes: 12- and 24-Week Phase 2 Studies. *Diabetes Care.* 2016;39(7):1241 - 9.
53. Kostic A, King TA, Yang F, Chan KC, Yancopoulos GD, Gromada J, et al. A first-in-human pharmacodynamic and pharmacokinetic study of a fully human anti-glucagon receptor monoclonal antibody in normal healthy volunteers. *Diabetes Obes Metab.* 2018;20(2):283-91.
54. Marroqui L, Masini M, Merino B, Grieco FA, Millard I, Dubois C, et al. Pancreatic α Cells are Resistant to Metabolic Stress-induced Apoptosis in Type 2 Diabetes. *EBioMedicine.* 2015;2(5):378 - 85.
55. Leite NC, Sintov E, Meissner TB, Brehm MA, Greiner DL, Harlan DM, et al. Modeling Type 1 Diabetes In Vitro Using Human Pluripotent Stem Cells. *Cell Rep.* 2020;32(2):107894.
56. Bosi E, Marchetti P, Rutter GA, and Eizirik DL. Human alpha cell transcriptomic signatures of types 1 and 2 diabetes highlight disease-specific dysfunction pathways. *Iscience.* 2022;25(10):105056.
57. Zhang P, McGrath B, Li Sa, Frank A, Zambito F, Reinert J, et al. The PERK eukaryotic initiation factor 2 alpha kinase is required for the development of the skeletal system, postnatal growth, and the function and viability of the pancreas. *Mol Cell Biol.* 2002;22(11):3864 - 74.
58. Akiyama M, Liew CW, Lu S, Hu J, Martinez R, Hambro B, et al. X-box binding protein 1 is essential for insulin regulation of pancreatic α-cell function. *Diabetes.* 2013;62(7):2439 - 49.
59. Bhattacharya A, and Qi L. ER-associated degradation in health and disease - from substrate to organism. *J Cell Sci.* 2019;132(23).

60. Bozadjieva N, Blandino-Rosano M, Chase J, Dai X-Q, Cummings K, Gimeno J, et al. Loss of mTORC1 signaling alters pancreatic α cell mass and impairs glucagon secretion. *J Clin Invest.* 2017;127(12):4379 - 93.
61. Shiota C, Prasadan K, Guo P, El-Gohary Y, Wiersch J, Xiao X, et al. α-Cells are dispensable in postnatal morphogenesis and maturation of mouse pancreatic islets. *American journal of physiology Endocrinology and metabolism.* 2013;305(8):E1030 - 40.
62. Kim K-S, Seeley RJ, and Sandoval DA. Signalling from the periphery to the brain that regulates energy homeostasis. *Nature Publishing Group.* 2018;19(4):185 - 96.
63. Zhu X, and Lindberg I. 7B2 facilitates the maturation of proPC2 in neuroendocrine cells and is required for the expression of enzymatic activity. *The Journal of cell biology.* 1995;129(6):1641-50.
64. Westphal CH, Muller L, Zhou A, Zhu X, Bonner-Weir S, Schambelan M, et al. The Neuroendocrine Protein 7B2 Is Required for Peptide Hormone Processing In Vivo and Provides a Novel Mechanism for Pituitary Cushing's Disease. *Cell.* 1999;96(5):689-700.
65. Leak TS, Keene KL, Langefeld CD, Gallagher CJ, Mychaleckyj JC, Freedman BI, et al. Association of the proprotein convertase subtilisin/kexin-type 2 (PCSK2) gene with type 2 diabetes in an African American population. *Mol Genet Metab.* 2007;92(1-2):145-50.
66. Zheng X, Ren W, Zhang S, Liu J, Li S, Li J, et al. Association of type 2 diabetes susceptibility genes (TCF7L2, SLC30A8, PCSK1 and PCSK2) and proinsulin conversion in a Chinese population. *Mol Biol Rep.* 2012;39(1):17-23.
67. Chang TJ, Chiu YF, Sheu WH, Shih KC, Hwu CM, Quertermous T, et al. Genetic polymorphisms of PCSK2 are associated with glucose homeostasis and progression to type 2 diabetes in a Chinese population. *Sci Rep.* 2015;5:14380.
68. Winters A, Ramos-Molina B, Jarvela TS, Yerges-Armstrong L, Pollin TI, and Lindberg I. Functional analysis of PCSK2 coding variants: A founder effect in the Old Order Amish population. *Diabetes Res Clin Pract.* 2017;131:82 - 90.
69. Campbell SA, Golec D, Hubert M, Johnson J, Salamon N, Barr A, et al. Human islets contain a subpopulation of glucagon-like peptide-1 secreting α cells that is increased in type 2 diabetes. *Molecular metabolism.* 2020:101014.
70. Holter MM, Saikia M, and Cummings BP. Alpha-cell paracrine signaling in the regulation of beta-cell insulin secretion. *Frontiers in Endocrinology.* 2022;13:934775.
71. Teitelman G. A Controversy Regarding the Identity of the Enzyme That Mediates Glucagon-Like Peptide 1 Synthesis in Human Alpha Cells. *Journal of Histochemistry & Cytochemistry.* 2024;72(8-9):545-50.
72. Rouille Y, Bianchi M, Irminger JC, and Halban PA. Role of the prohormone convertase PC2 in the processing of proglucagon to glucagon. *Febs Lett.* 1997;413(1):119-23.

73. Wei X, Lu Y, Lin LL, Zhang C, Chen X, Wang S, et al. Proteomic screens of SEL1L-HRD1 ER-associated degradation substrates reveal its role in glycosylphosphatidylinositol-anchored protein biogenesis. *Nature Communications.* 2024;15(1):659.
74. Wang HH, Lin LL, Li ZJ, Wei X, Askander O, Cappuccio G, et al. Hypomorphic variants of SEL1L-HRD1 ER-associated degradation are associated with neurodevelopmental disorders. *Journal of Clinical Investigation.* 2023;134(2):e170054.
75. Kaestner KH, Powers AC, Naji A, Consortium H, and Atkinson MA. NIH Initiative to Improve Understanding of the Pancreas, Islet, and Autoimmunity in Type 1 Diabetes: The Human Pancreas Analysis Program (HPAP). *Diabetes.* 2019;68(7):1394-402.
76. Shapira SN, Naji A, Atkinson MA, Powers AC, and Kaestner KH. Understanding islet dysfunction in type 2 diabetes through multidimensional pancreatic phenotyping: The Human Pancreas Analysis Program. *Cell Metab.* 2022;34(12):1906-13.
77. Brissova M, Niland JC, Cravens J, Olack B, Sowinski J, and Evans-Molina C. The Integrated Islet Distribution Program Answers the Call for Improved Human Islet Phenotyping and Reporting of Human Islet Characteristics in Research Articles. *Diabetes.* 2019;68(7):1363 - 5.
78. Kong Y, Ebrahimpour P, Liu Y, Yang C, and Alonso LC. Pancreatic Islet Embedding for Paraffin Sections. *J Vis Exp.* 2018(136).
79. Dai C, Brissova M, Hang Y, Thompson C, Poffenberger G, Shostak A, et al. Islet-enriched gene expression and glucose-induced insulin secretion in human and mouse islets. *Diabetologia.* 2012;55(3):707 - 18.
80. Brissova M, Fowler M, Wiebe P, Shostak A, Shiota M, Radhika A, et al. Intraislet endothelial cells contribute to revascularization of transplanted pancreatic islets. *Diabetes.* 2004;53(5):1318-25.
81. Reinert RB, Cai Q, Hong J-Y, Plank JL, Aamodt K, Prasad N, et al. Vascular endothelial growth factor coordinates islet innervation via vascular scaffolding. *Development.* 2014;141(7):1480 - 91.
82. Ji Y, Sun S, Shrestha N, Darragh LB, Shirakawa J, Xing Y, et al. Toll-like receptors TLR2 and TLR4 block the replication of pancreatic β cells in diet-induced obesity. *Nat Immunol.* 2019;20(6):677 - 86.
83. Okita N, Higami Y, Fukai F, Kobayashi M, Mitarai M, Sekiya T, et al. Modified Western blotting for insulin and other diabetes-associated peptide hormones. *Scientific reports.* 2017;7(1):6949.
84. Sha H, He Y, Chen H, Wang C, Zenno A, Shi H, et al. The IRE1alpha-XBP1 pathway of the unfolded protein response is required for adipogenesis. *Cell Metab.* 2009;9(6):556-64.
85. Abramson J, Adler J, Dunger J, Evans R, Green T, Pritzel A, et al. Accurate structure prediction of biomolecular interactions with AlphaFold 3. *Nature.* 2024;630(8016):493-500.

SUPPLEMENTAL TABLES

Table S1. Characteristics from islet donors.

	HPAP035 "No DM"	**ICRH121 "T2DM"**
Donor age (years)	35	54
Donor sex	Male	Male
Donor ethnicity	Caucasian	African-American
Donor BMI (kg/m^2)	26.9	33.7
Donor HbA1c (%)	5.2	8.0
Donor diagnosis	No diabetes	Type 2 diabetes for two years
Donor cause of death	Anoxia	Cerebrovascular accident

Table S2. CRISPR-targeting sgRNA oligonucleotides

Gene Name (Protein Name)	**Forward Sequence (5'→3')**	**Reverse Sequence (5'→3')**
Sel1L (SEL1L)	CACCGGCCAGCAACTACTTTGCCCG	AAACCGGGCAAAGTAGTTGCTGGCC
Hrd1 (HRD1)	CACCGATCCATGCGGCATGTCGGGC	AAACGCCCGACATGCCGCATGGATC
Pcsk2 (PC2)	CACCGACCAGTCATCTGTGTATCGA	AAACTCGATACACAGATGACTGGTC

Table S3. Primer sequences for PCR.

Gene Name (Protein Name)	**Forward Sequence (5'→3')**	**Reverse Sequence (5'→3')**
L32	GAGCAACAAGAAAACCAAGCA	TGCACACAAGCCATCTACTCA
Rplp0 (36B4)	AGATTCGGGATATGCTGTTGGC	TCGGGTCCTAGACCAGTGTTC
Xbp1, spliced	TTACGAGAGAAAACTCATGGGC	GGGTCCAACTTGTCCAGAATGC
Pcsk2	AGAGAGACCCCAGGATAAAGATG	CTTGCCCAGTGTTGAACAGGT

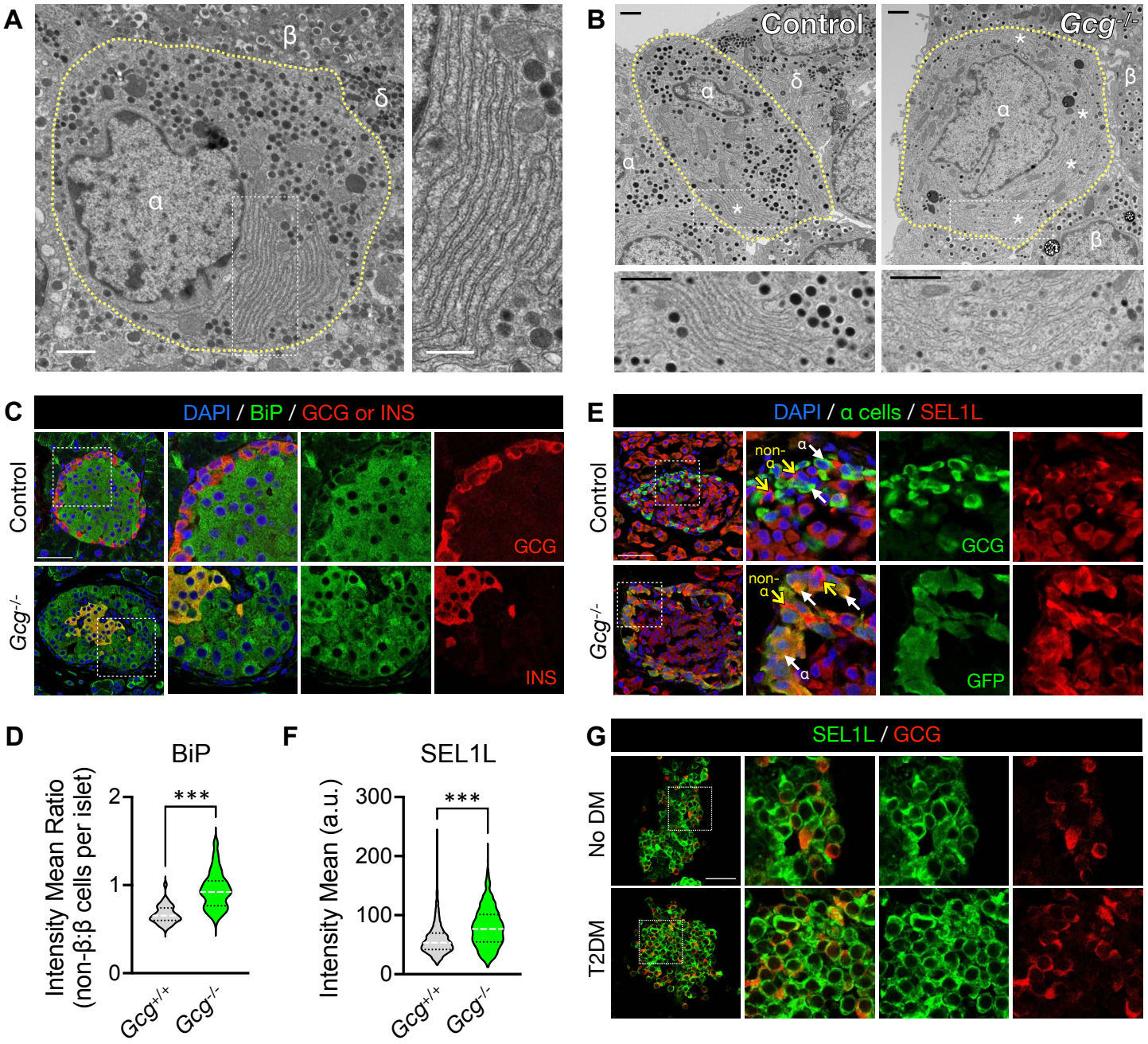

Figure 1. The endoplasmic reticulum (ER) is a prominent feature of normal and proliferative islet α cells. A, Transmission electron microscopy (TEM) image of a normal α cell (yellow dashed outline), demonstrating prominent stacks of rough ER. Adjacent β and δ cells are labeled. Scale bar of left panel, 1 μm; of inset, 600 nm. B, TEM images showing prominent ER stacks (asterisks) in highly proliferative α cells from *Gcg*$^{-/-}$ mice compared to littermate controls. Scale bars, 1 μm. Additional TEM images are shown in Figure S1A. C, Representative islets from *Gcg*$^{-/-}$ mice and littermate controls, immunolabeled for the ER chaperone BiP and either glucagon (GCG, top panels) or insulin (INS, bottom panels). D, Violin plot shows the distribution of relative BiP immunofluorescence in islets from *Gcg*$^{-/-}$ and control mice, quantified as the ratio of the average BiP intensity of non-β cells to β cells. Data represents a total of 37-61 islets from *n* = 3-4 mice per genotype, with median line shown in white and quartile lines in black. ***$P < 0.001$, unpaired two-tailed Student's t test. E, Representative islet cryosections immunolabeled for the ER-associated degradation (ERAD) component SEL1L and either glucagon (GCG, top panels) or GFP (as expressed by the construct inserted into the Gcg gene, bottom panels). White arrows mark examples of α cells. Yellow arrows denote peripheral non-α islet cells that highly express SEL1L, notably with absence of glucagon expression. F, Violin plot shows the distribution of SEL1L immunofluorescence in GCG+ or GFP+ α cells, normalized to the mean intensity of SEL1L in β cells within the same islet. Data represents a total of 1400-2300 α cells from *n* = 3-4 mice per genotype, with median line shown in white and

quartile lines in black. ***$P < 0.001$, unpaired two-tailed Student's t test. G, Cryosections of isolated islets from human islet donors immunolabeled for SEL1L and glucagon (GCG). The islet in the top panels is from a donor without diabetes (No DM), and the islet in the bottom panels is from a donor with a two-year history of type 2 diabetes (T2DM); see Table S1 for further donor characteristics. Scale bar for left panels in C-E, 50 μm.

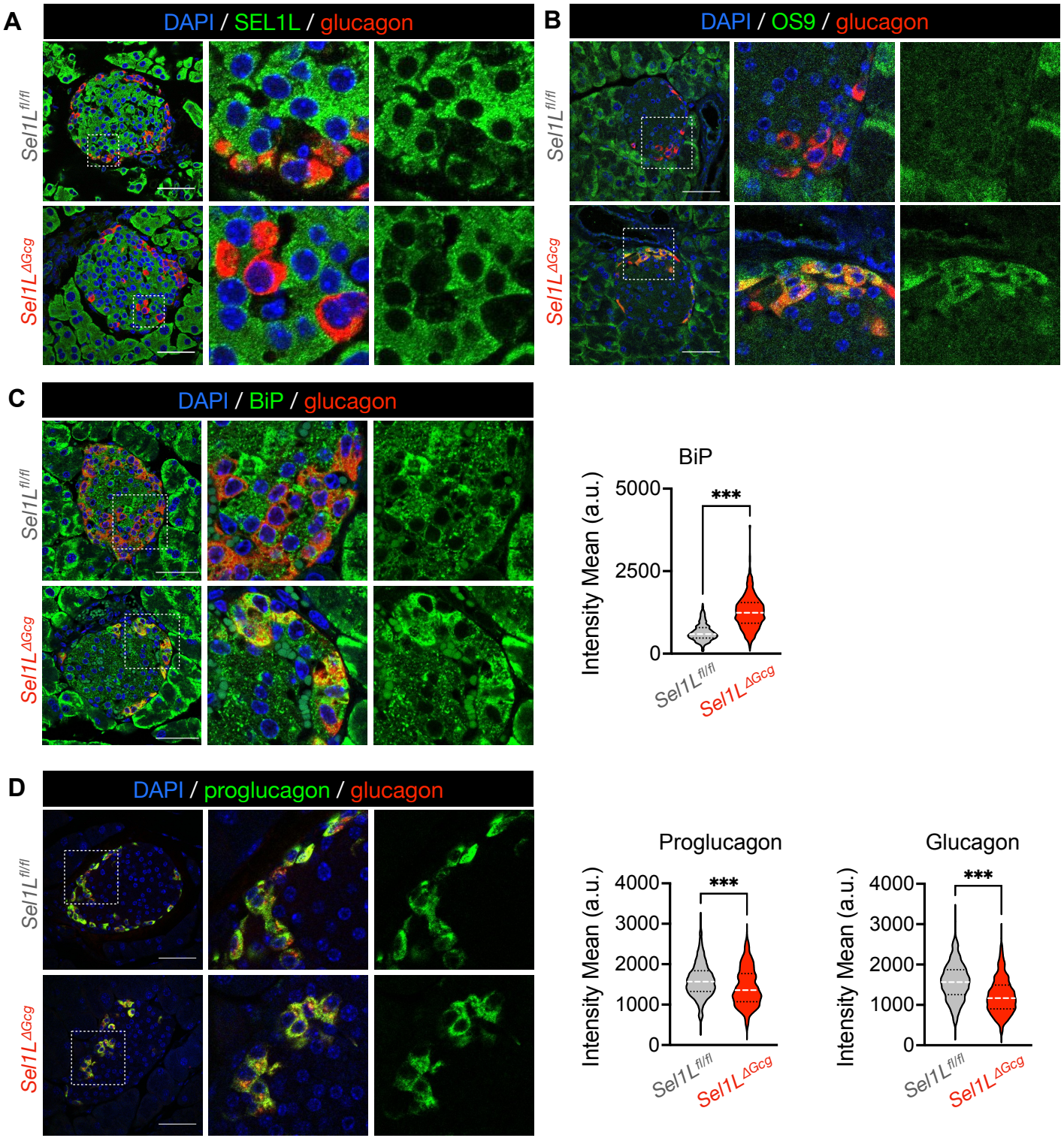

Figure 2. Inactivation of SEL1L-HRD1 ERAD disrupts ER homeostasis in α cells but does not lead to accumulation of proglucagon-derived peptides. Representative islets from adult (4-8 month-old) *Sel1L*$^{\Delta Gcg}$ mice and *Sel1L*$^{fl/fl}$ littermate controls, immunolabeled for glucagon and the ERAD component SEL1L (A), the ERAD cofactor/substrate OS9 (B), the ER chaperone BiP (C), or proglucagon (D). Scale bars of left panels, 50 μm. Violin plots show the distribution of immunofluorescence intensity of BiP, proglucagon, or glucagon in 500-1300 α cells from *n* = 3-4 mice per genotype, with median line shown in white and quartile lines in black. ***$P < 0.001$, unpaired two-tailed Student's t test.

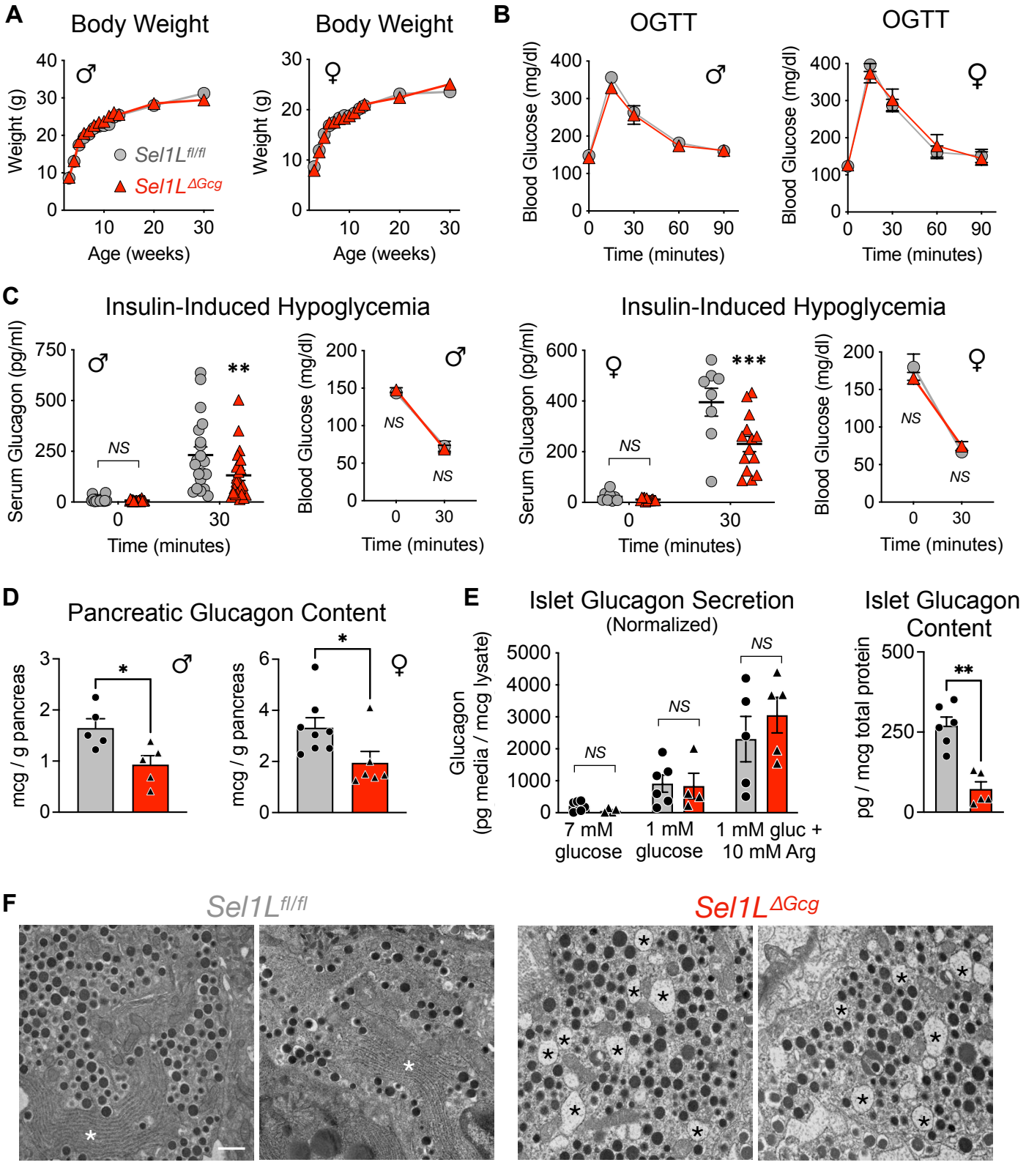

Figure 3. ERAD inactivation in α cells does not affect systemic growth or glucose tolerance but limits glucagon production with age. A-B, Body weight and oral glucose tolerance (OGTT) in adult (4-8 month-old) male and female *Sel1L*$^{\Delta Gcg}$ mice (red triangles) and *Sel1L*$^{fl/fl}$ controls (gray circles). Each data point represents $n > 6$ mice, shown as mean ± SEM. C, Serum glucagon and glucose levels *in vivo* in adult male (>4 months) and female (>8 months) *Sel1L*$^{\Delta Gcg}$ mice (red triangles) and *Sel1L*$^{fl/fl}$ controls (gray circles) in response to insulin-induced

hypoglycemia. For serum glucagon, each data point represents data from one mouse, with mean ± SEM bars shown; for blood glucose, data represents mean ± SEM. D, Acid ethanol-extracted pancreatic glucagon content in adult (4-8 month-old) mice. Each data point represents data from one mouse, with mean ± SEM shown. E, Normalized glucagon secretion and total islet glucagon content from isolated *Sel1L*$^{\Delta Gcg}$ and *Sel1L*$^{fl/fl}$ islets. Each data point represents data from one mouse, with mean ± SEM shown. F, Representative transmission electron microscopy images of α cells from adult *Sel1L*$^{\Delta Gcg}$ mice and *Sel1L*$^{fl/fl}$ controls, with ER stacks or dilated ER lumen denoted by asterisks. Scale bar, 600 nm. *P < 0.05, **P < 0.01, ***P < 0.001; *NS*, not significant with P > 0.05; a two-way ANOVA with Šidák post-test was performed for serum glucagon tests in C, and an unpaired two-tailed Student's t test was performed to compare groups in all other graphs.

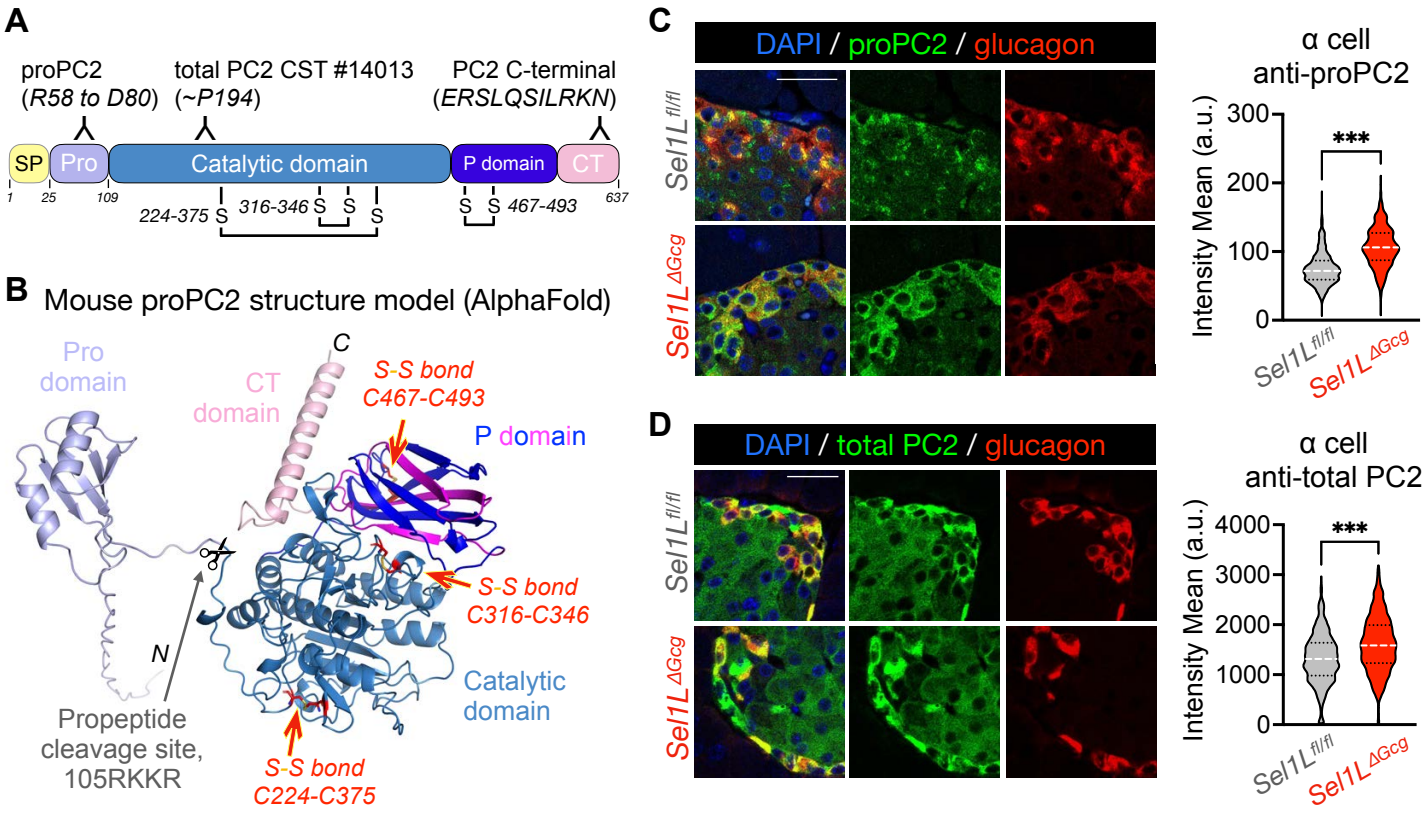

Figure 4. Inactivation of SEL1L-HRD1 ERAD in α cells leads to accumulation of prohormone convertase 2 in vivo. A, Schematic diagram of the mouse preproPC2 peptide, denoting the locations of antibody targets. SP, signal peptide; Pro, propeptide; CT, C-terminal region. B, AlphaFold 3 structural model of the mouse proPC2 peptide. C-D, Representative islets from *Sel1L*$^{\Delta Gcg}$ mice and *Sel1L*$^{fl/fl}$ controls, immunolabeled for the PC2 propeptide (C) or total prohormone convertase 2 (PC2 CST, D). Scale bars, 25 µm. Violin plots at right show the distribution of immunofluorescence intensity of (pro)PC2 in glucagon+ cells from 800-1300 cells with n = 3-4 mice per genotype, with median line shown in white and quartile lines in black. ***P < 0.001; unpaired two-tailed Student's t test.

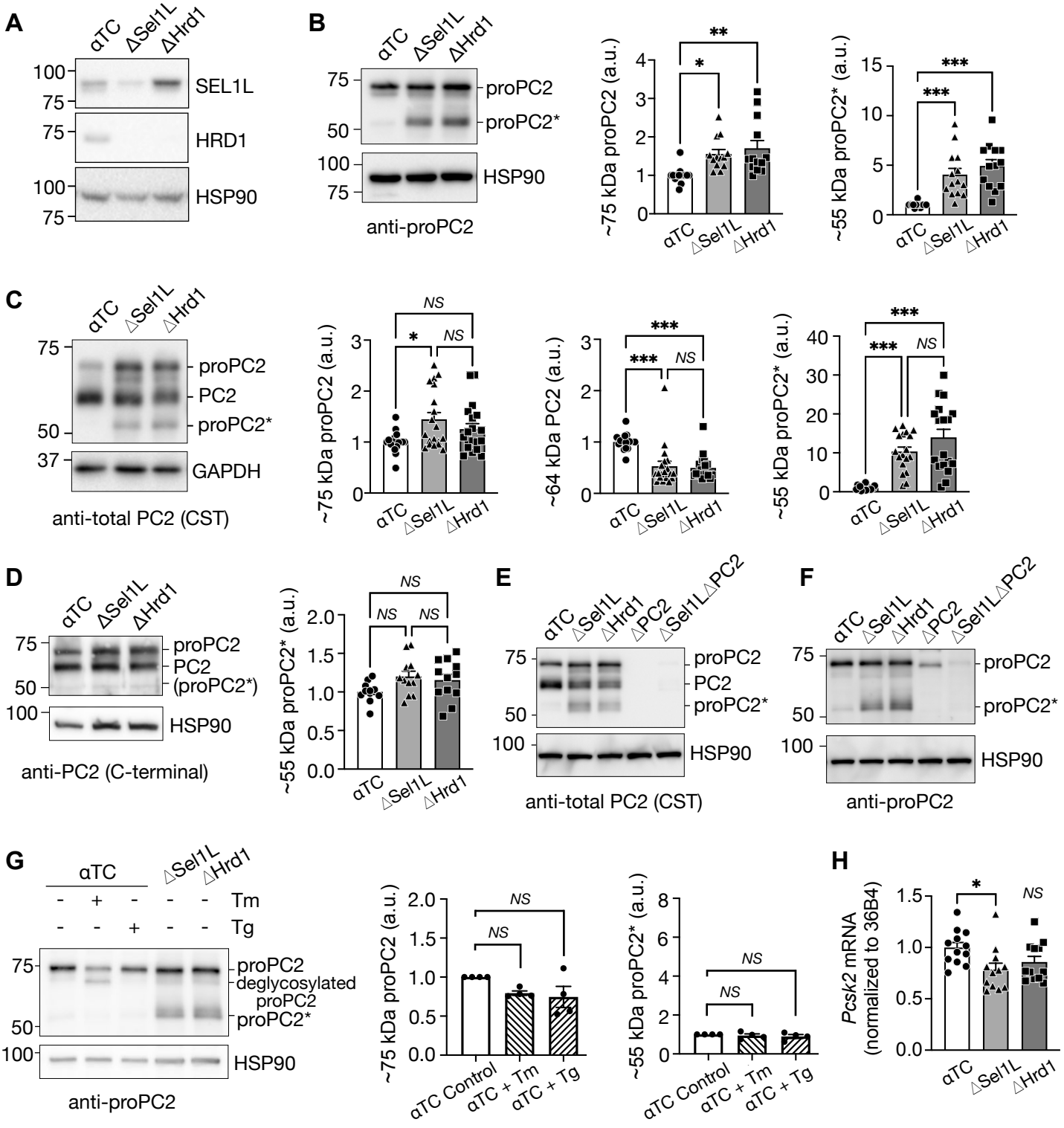

Figure 5. Inactivation of SEL1L-HRD1 ERAD in α cells alters processing of prohormone convertase 2. A, Western blot of SEL1L and HRD1 expression in αTC1-6 cells following CRISPR-mediated deletion of Sel1L (ΔSel1L) or Hrd1 (ΔHrd1) compared to vector-treated controls (αTC). B-D, Western blots of αTC cells using antibodies to the PC2 propeptide (B), PC2 catalytic domain (C), or PC2 C-terminal domain (D), with band quantification shown at right. Note the generation of an N-terminal fragment of the proPC2 peptide in ΔSel1L and ΔHrd1 cells, denoted proPC2*. E-F, Western blot of αTC cells following CRISPR-mediated deletion of SEL1L (ΔSel1L), HRD1 (ΔHrd1), and/or PC2 (ΔPC2), labeled with antibodies to the catalytic domain of PC2 (E) or to the PC2 propeptide (F). G, Western blot of tunicamycin

(Tm)- and thapsigargin (Tg)-treated control αTC cells, labeled with an antibody to proPC2, with band quantification shown at right. H, Quantitative RT-PCR of the *Pcsk2* gene encoding PC2 in αTC cells. In bar graphs, each data point represents a single replicate, shown as mean ± SEM. **P* < 0.05; ***P* < 0.01; ****P* < 0.001; *NS*, not significant (*P* > 0.05); one-way ANOVA with Šidák post-test.

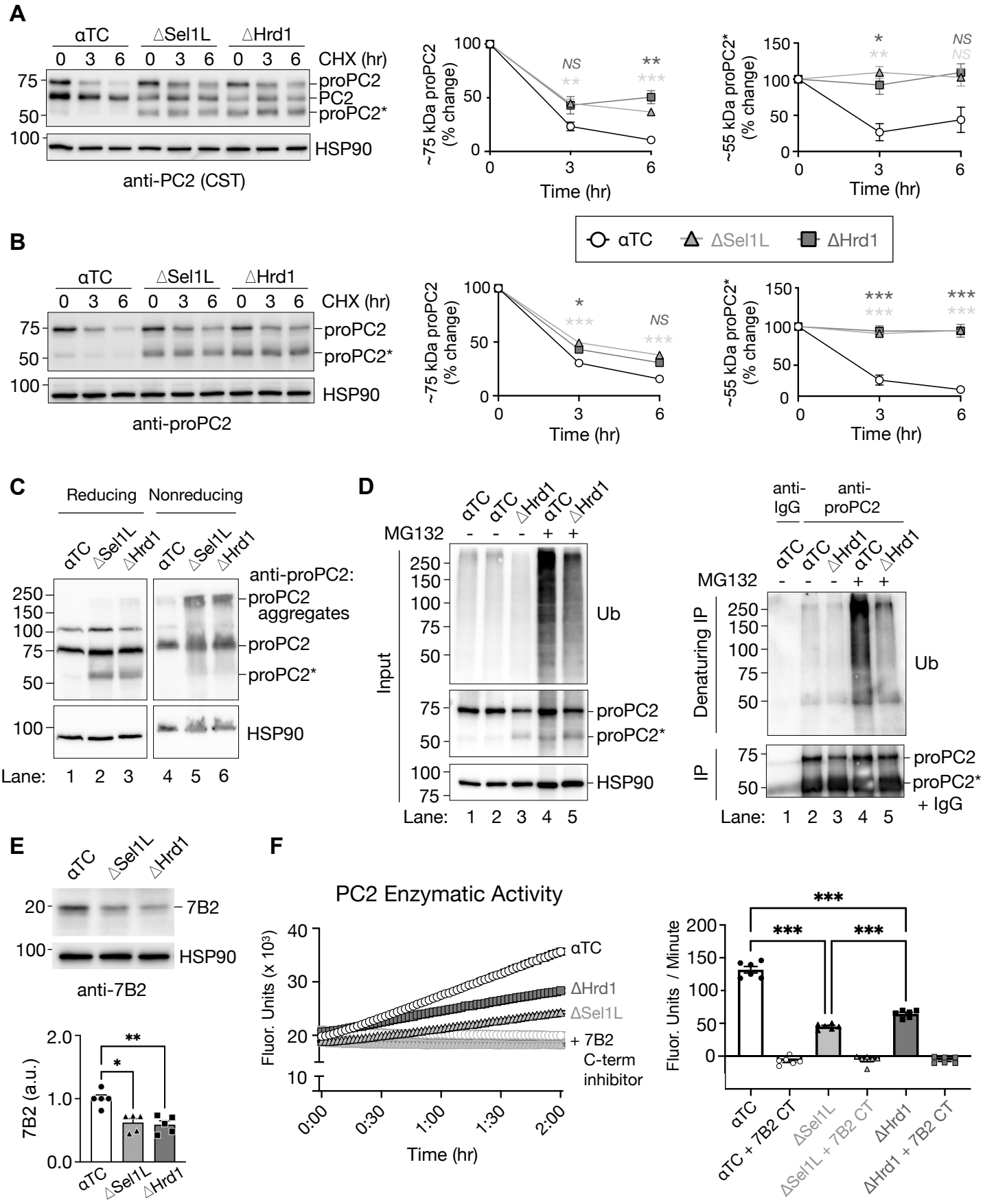

Figure 6. Inactivation of SEL1L-HRD1 ERAD in α cells alters processing of prohormone convertase 2. A-B, Western blot of αTC cells following 0, 3, and 6 hours of treatment with cycloheximide (CHX) to inhibit new protein synthesis, labeled with antibodies targeting the cai n of PC2 (CST, A) or proPC2 (B). Quantification of the relative expression of each (pro)PC2 form over time is shown at right (data points are averages of $n = 2$ replicates from three independent experiments, shown as mean ± SEM). C, Western blot of αTC cell lysates prepared under reducing and nonreducing conditions, labeled with antibodies to proPC2. Note that images from reducing and nonreducing conditions are from the same blot, cropped for clarity. D, Western blot analysis of protein ubiquitination before (Input, left) and after (Denaturing IP, right) immunoprecipitation with antibodies to proPC2 or IgG control in αTC and ΔHrd1 cells. E, Western blot and quantification of the proPC2 chaperone protein 7B2 in αTC, ΔSel1L, and ΔHrd1 cells. Each data point represents a single replicate, shown as mean ± SEM. F, PC2 enzymatic activity of cell lysates as measured by a substrate-specific aminomethylcoumarin assay, performed with and without the addition of exogenous 7B2 C-terminal (CT) peptide as a specific PC2 inhibitor. In the time course graph, each data point represents the mean ± SEM of six replicates. In the bar graph, each data point represents the rate of change in fluorescence intensity for individual replicates in the time course graph, shown as mean ± SEM. For each graph, $*P < 0.05$; $**P < 0.01$; $***P < 0.001$; *NS*, not significant ($P > 0.05$); one-way ANOVA with Šidák post-test.

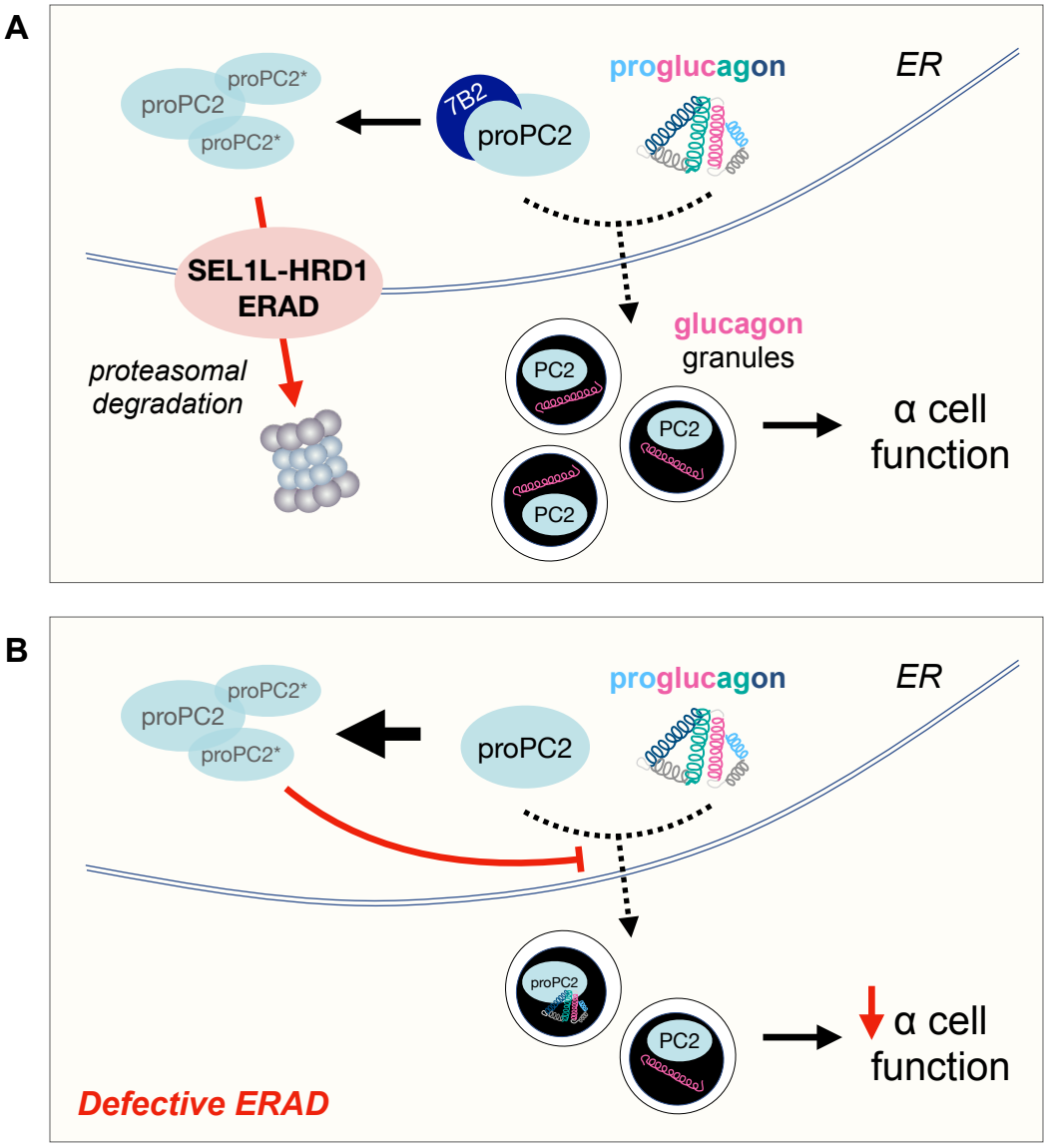

Figure 7. Working model. A, SEL1L-HRD1 ERAD is a critical ER protein quality control pathway in α cells, targeting misfolded and/or aggregated pro-prohormone convertase 2 (proPC2) and aberrantly cleaved proPC2* molecules for proteasomal degradation. SEL1L-HRD1 ERAD function is essential to allow for packaging of properly folded proPC2 and proglucagon into secretory granules, where proPC2 is then activated into the functional PC2 enzyme that cleaves proglucagon into glucagon - thus promoting α cell function. B, Defective SEL1L-HRD1 ERAD function in α cells leads to aggregation of proPC2 and aberrantly cleaved proPC2*, limiting the packaging of activation-competent proPC2 into secretory granules and thus limiting the production of mature glucagon.

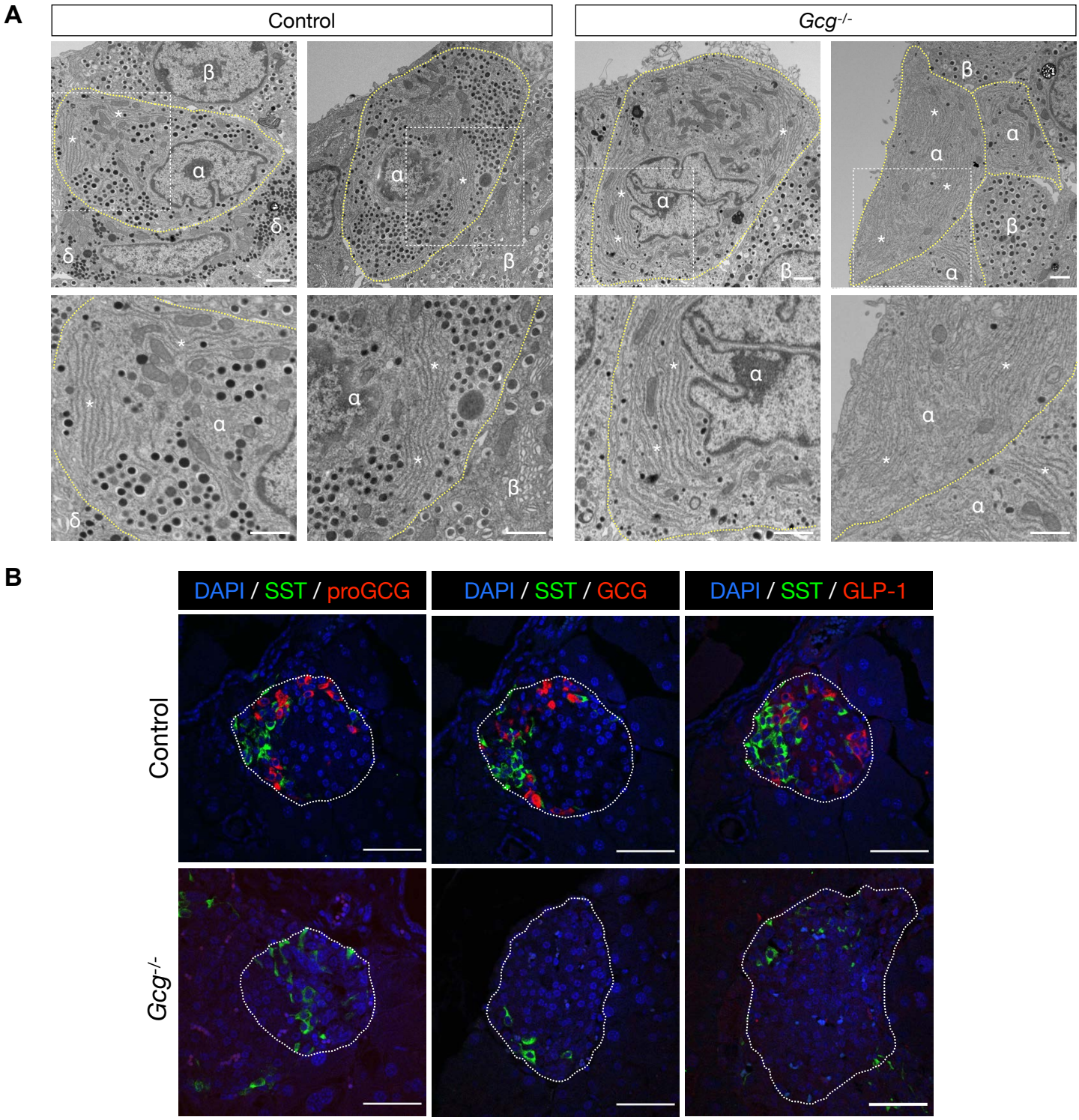

Supplemental Figure S1. The endoplasmic reticulum (ER) is a prominent feature of normal and proliferative α cells. A, Rough ER (asterisks) in α cells (yellow dashed lines) from *Gcg*-STOP-flox (*Gcg*$^{-/-}$) mice and littermate controls. Scale bars, 1 μm. B, Representative islets from *Gcg*$^{-/-}$ mice and controls, immunolabeled for somatostatin (SST; labeling islet δ cells) and proglucagon (proGCG), glucagon (GCG), or GLP-1. Islet borders are outlined. Scale bars, 50 μm.

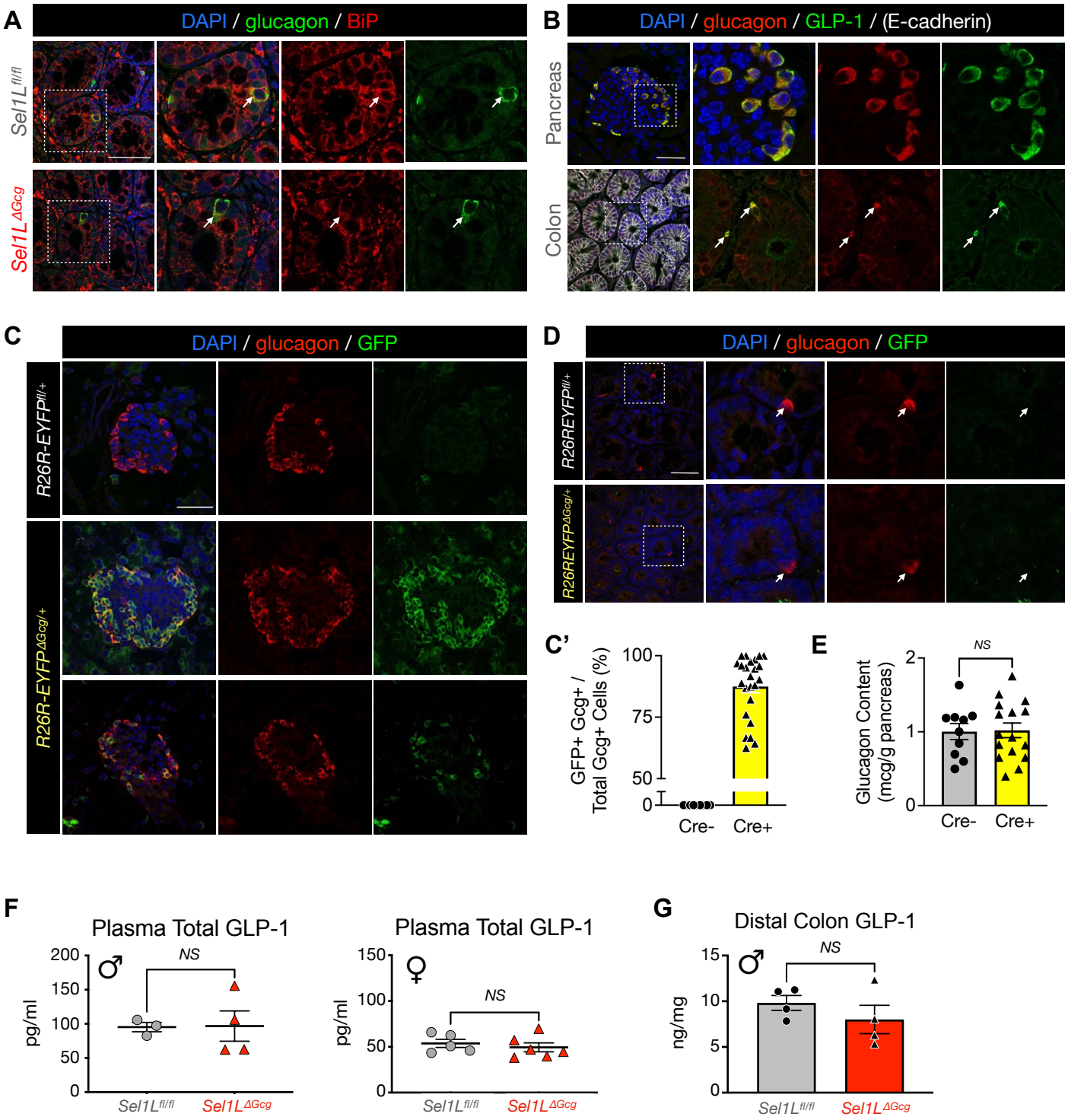

Supplemental Figure S2. *Gcg*-iCre mice show effective recombination in islet α cells but not intestinal L-cells. A, Colon from *Sel1L*$^{\Delta Gcg}$ mice and *Sel1L*$^{fl/fl}$ littermate controls, immunolabeled with antibodies to glucagon and BiP. B, Representative section from pancreas and colon from control mice immunolabeled with antibodies to glucagon and GLP-1, along with E-cadherin in the colon sample. Note the similarities in labeling suggest that both antibodies also bind to the full-length proglucagon peptide. C, Representative islets from *R26R-EYFP*$^{\Delta Gcg/+}$ (Cre +) mice and *R26R-EYFP*$^{fl/+}$ (Cre -) controls, immunolabeled with antibodies to glucagon and GFP; quantification of GFP+ α cells is shown in C' with each data point representing one islet. D, Intestinal cryosections from *R26R-EYFP*$^{\Delta Gcg/+}$ mice and Cre-negative *R26R-EYFP*$^{fl/+}$ controls, immunolabeled with antibodies to (pro)glucagon and GFP. Scale bars, 50 μm. E, Pancreatic glucagon content in *R26R-EYFP*$^{\Delta Gcg/+}$ (Cre +) mice and *R26R-EYFP*$^{fl/+}$ (Cre -) controls at 6-13 weeks of

age, mixed sexes. Each data point represents one mouse. F, Plasma total GLP-1 (1-26, 7-36, and 9-36) levels following glucose administration in male and female *Sel1L*$^{\Delta Gcg}$ mice and *Sel1L*$^{fl/fl}$ controls. G, Total GLP-1 extracted from distal colon epithelium in male *Sel1L*$^{\Delta Gcg}$ mice and *Sel1L*$^{fl/fl}$ controls. For F-G, each data point represents one mouse. *NS*, not significant ($P > 0.05$), unpaired two-tailed Student's t test. Data represent mean ± SEM.

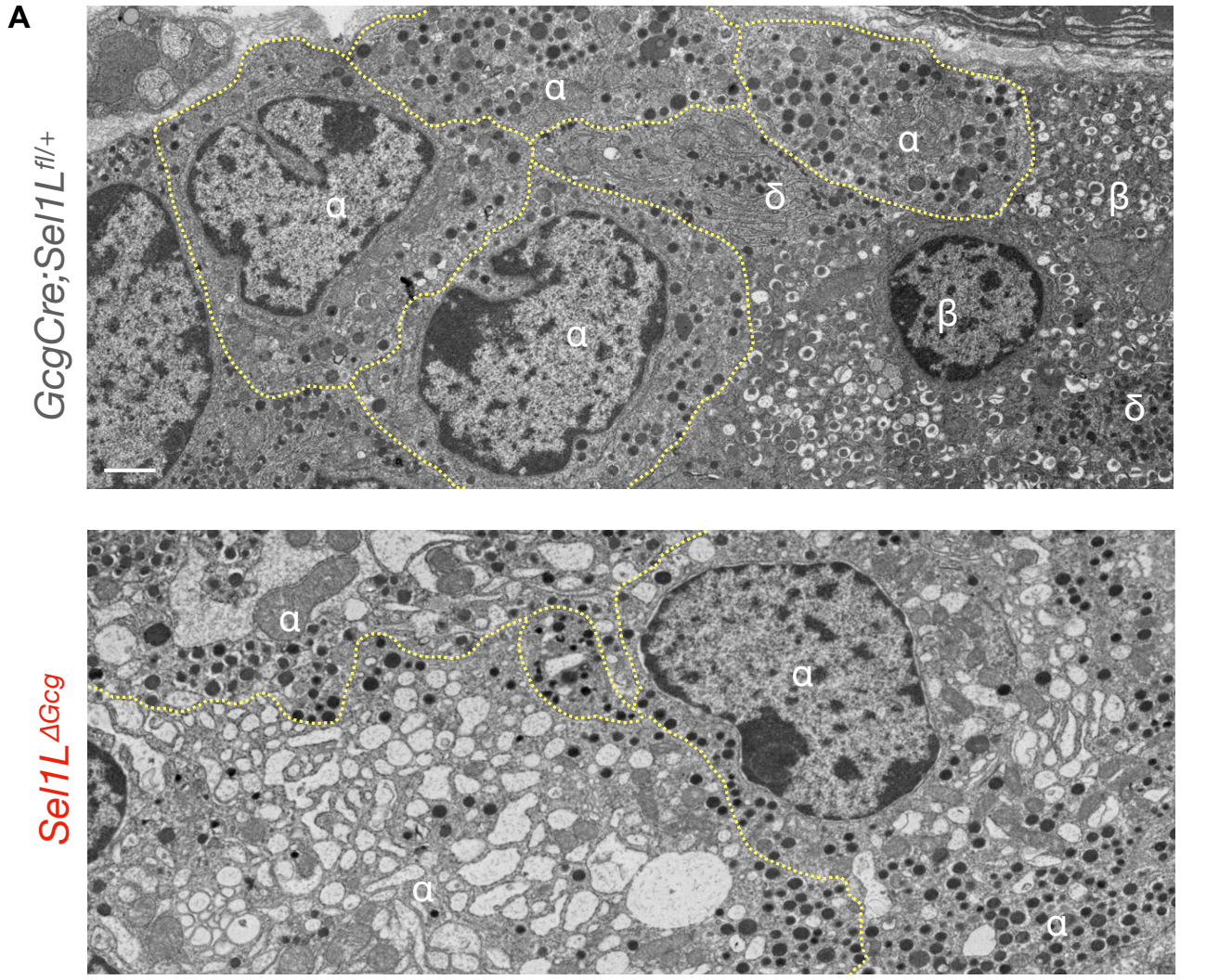

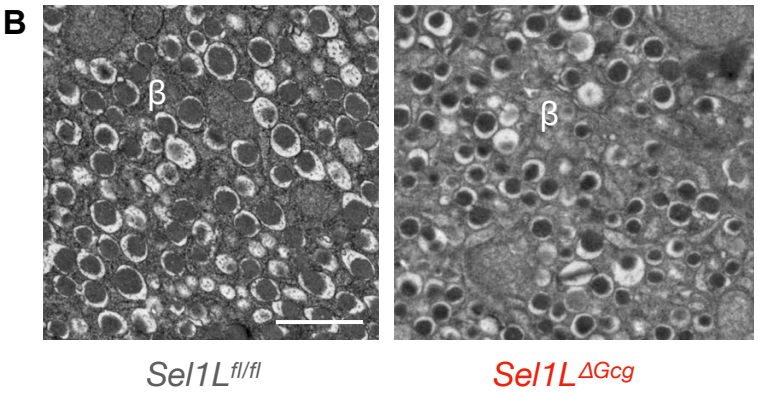

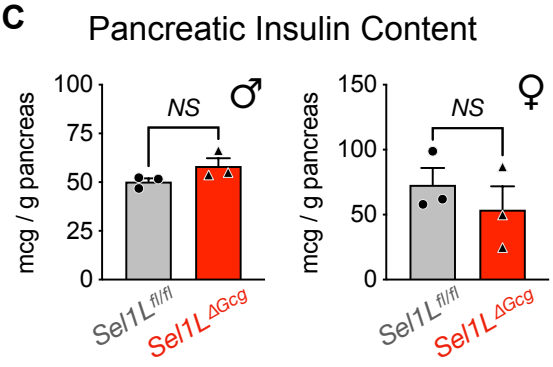

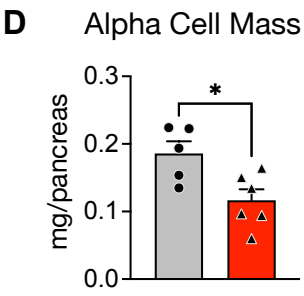

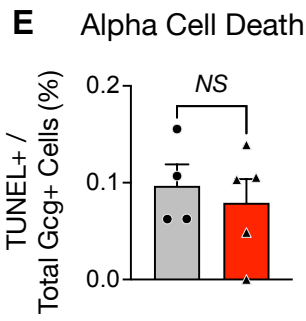

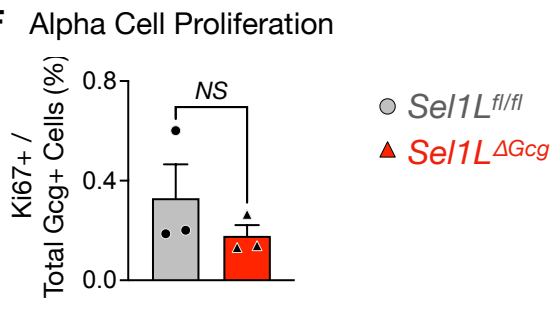

Supplemental Figure S3. SEL1L inactivation in pancreatic α cells disrupts ER morphology and glucagon production but does not affect β cell morphology or function. A, Transmission electron microscopy (TEM) of pancreatic islets from an aged *Sel1L*$^{\Delta Gcg}$ mouse and littermate control. B, TEM of representative β cells from each genotype. Scale bars in A-B, 1 μm. C, Acid-alcohol extracted pancreatic insulin content in male and female *Sel1L*$^{\Delta Gcg}$ mice and *Sel1L*$^{fl/fl}$ controls. D-F, Alpha cell mass (D), TUNEL labeling for α cell apoptosis (E), and Ki67+ α cell proliferation (F) in adult (4-8 month-old) *Sel1L*$^{\Delta Gcg}$ mice and *Sel1L*$^{fl/fl}$ controls. In graphs, each point represents data from one mouse, shown as mean ± SEM. **P* < 0.05, *NS*, not significant with *P* > 0.05; unpaired two-tailed Student's t test.

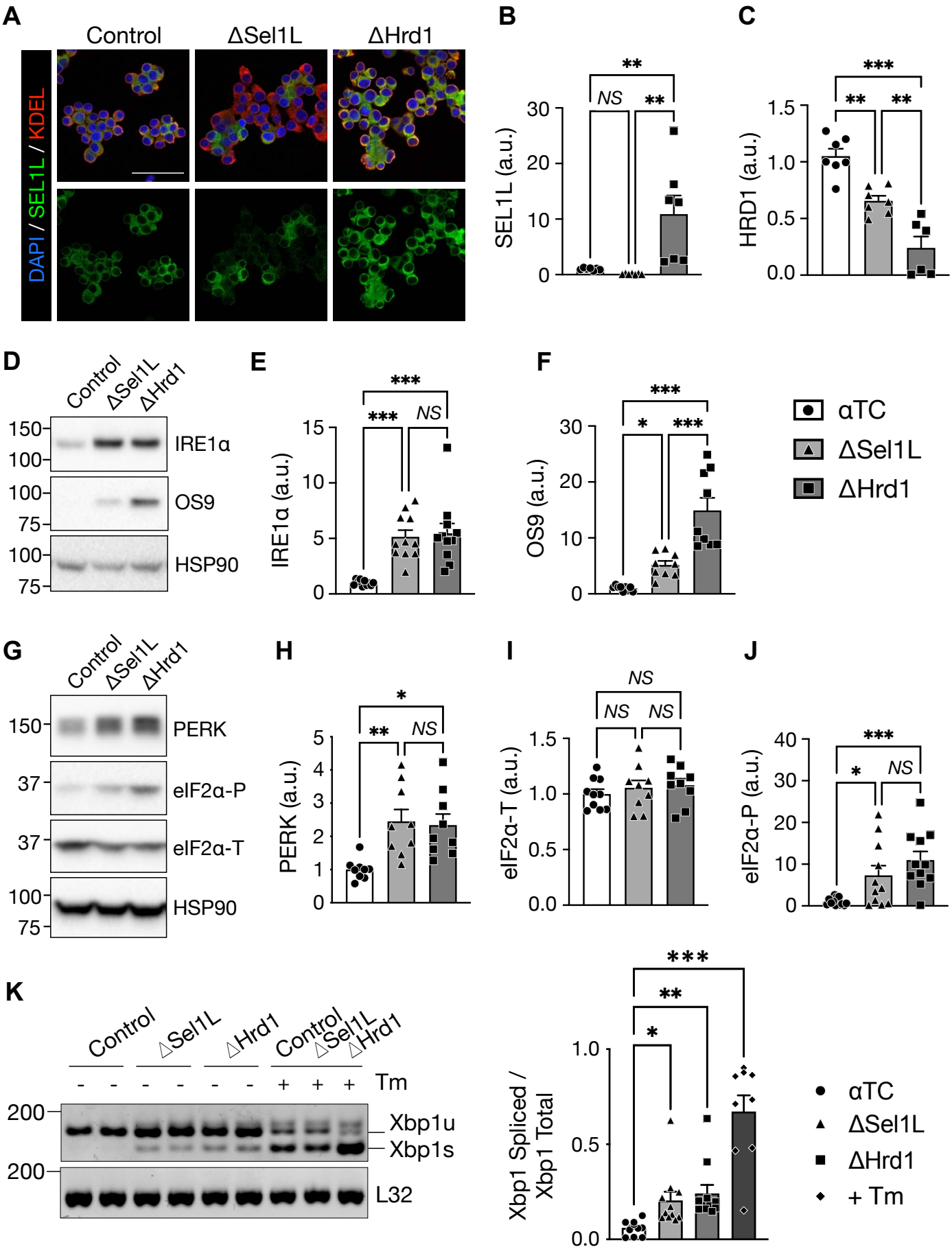

Supplemental Figure S4. Inactivation of SEL1L or HRD1 in αTC cells leads to mild activation of the unfolded protein response in vitro. A, Immunofluorescence of αTC1-6 cells following CRISPR-mediated deletion of Sel1L (ΔSel1L) or Hrd1 (ΔHrd1) compared to vector-treated controls, labeled for Sel1L and the ER marker KDEL. Note that deletion of Sel1L was incomplete, so Hrd1 deletion was used as an alternative means to inactivate ERAD function. Scale bar, 50 μm. B-C, Quantification of SEL1L (B) and HRD1 (C) protein expression in αTC1-6 cells following CRISPR-mediated deletion of SEL1L (ΔSel1L, light gray/triangles) or HRD1 (ΔHrd1, dark gray/squares) compared to vector-treated αTC controls (white/circles). Representative Western blots are shown in Fig. 4D. D-F, Western blots and quantification of ERAD substrate and UPR sensor IRE1α, and ERAD substrate OS9, in αTC cells with targeted deletion of SEL1L or HRD1. Note that the HSP90 loading control is identical to that shown in Fig. 4D. G-J, Western blots and quantification of UPR sensor PERK and its downstream effector eIF2α (P, phosphorylated; T, total) in αTC cells with targeted deletion of SEL1L or HRD1. Western blot experiments were performed at least three times, with each data point in graphs representing individual replicates and summary bars shown as mean ± SEM, expressed as arbitrary units (a.u.). K, RT-PCR detection of *Xbp1* mRNA in unspliced (Xbp1u) and spliced (Xbp1s) forms. Quantification was calculated as the ratio of Xbp1s to total Xbp1 (n = 1-3 x 5 experiments), with each data point in graph representing individual replicates and summary bars shown as mean ± SEM. Tunicamycin (Tm) treatment was used as a positive control for activation of IRE1α-mediated Xbp1 splicing; the "αTC + Tm" group is an aggregate of Tm-treated replicates from each genotype. *P < 0.05, **P < 0.01, ***P < 0.001, *NS*, not significant (P > 0.05); one-way ANOVA with Šidák post-test.